ESC-TR-98-052

Technical Report
1053

Fourier Transform Interferometry

D.R. Hearn

29 October 1999

Lincoln Laboratory
MASSACHUSETTS INSTITUTE OF TECHNOLOGY
LEXINGTON, MASSACHUSETTS

Prepared for the National Oceanic and Atmospheric Administration
under Air Force Contract F19628-95-C-0002.

This report is based on studies performed at Lincoln Laboratory, a center for research operated by Massachusetts Institute of Technology. This work was sponsored by the National Oceanic and Atmospheric Administration under Air Force Contract F19628-95-C-0002.

The ESC Public Affairs Office has reviewed this report, and it is releasable to the National Technical Information Service, where it will be available to the general public, including foreign nationals.

This technical report has been reviewed and is approved for publication.

FOR THE COMMANDER

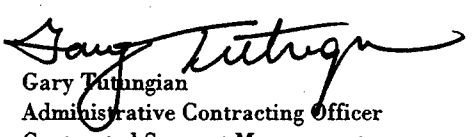

Gary Tutungian
Administrative Contracting Officer
Contracted Support Management

MASSACHUSETTS INSTITUTE OF TECHNOLOGY
LINCOLN LABORATORY

FOURIER TRANSFORM INTERFEROMETRY

D.R. HEARN
Group 96

TECHNICAL REPORT 1053

29 OCTOBER 1999

LEXINGTON MASSACHUSETTS

ABSTRACT

The basic Michelson interferometer, as used for Fourier transform spectroscopy, is analyzed in this report. The principles of operation are explained, and its inherent limitations are shown. An original analysis of apodization, for the case of an off-axis detector field-of-view, is included in an appendix. Practical limitations of real instruments are also analyzed. These include misalignment, wavefront error, and noise sources. In another appendix, the use of retroreflectors in the interferometer is analyzed, and the effect of lateral displacement of a retroreflector is compared to that of mirror tilt in a plane-mirror interferometer. Special attention is given to sources of noise in the Fourier transform spectroradiometer, and expressions are derived for noise-equivalent radiance from these sources. The performance of a Fourier transform spectrometer is compared with that of a filter-wheel spectrometer having the same optical aperture and spectral resolution. The mathematical treatments in this report are sufficiently detailed that they should be easy to follow, once the optical principles are grasped. Some numerical calculations are included, based on the specifications of the proposed GOES High-Resolution Interferometer Sounder (GHIS).

ACKNOWLEDGMENTS

The author wishes to acknowledge the support of the National Oceanic and Atmospheric Administration, which sponsored this work. This report was stimulated in part by the work on atmospheric sounding by Prof. William Smith and Dr. Hank Revercomb of the University of Wisconsin. Discussions with Lincoln Laboratory staff members were helpful on particular points. Those individuals include Dr. W. E. Bicknell, Dr. L. M. Candell, Dr. D. L. Mooney, M. J. Persky, Dr. A. B. Plaut, and Dr. D. P. Ryan-Howard. Dr. Bicknell was particularly helpful in pointing out the Lommel function solution for the integral encountered in calculating the apodization for a detector not on the interferometer axis.

TABLE OF CONTENTS

Abstract iii
Acknowledgments v
List of Illustrations ix
List of Symbols Used xi

1. INTRODUCTION 1

2. PRINCIPLE OF OPERATION 3

3. INHERENT LIMITATIONS 7
   3.1 Resolution 7
   3.2 Apodization 7
   3.3 Throughput 11

4. PRACTICAL LIMITATIONS 13
   4.1 Misalignment 13
   4.2 Wavefront Errors 14
   4.3 Splitter-Compensator Differences 17
   4.4 Noise Sources 18
      4.4.1 Conversion from Interferogram to Spectral Domain 18
      4.4.2 Noise-Equivalent Spectral Radiance 19
      4.4.3 Photon and Detector Noise 20
      4.4.4 Electronics Noise 21
      4.4.5 Aliased Noise 22
      4.4.6 Low-Frequency ("1/*f*") Noise 22
      4.4.7 Quantization Noise 23
      4.4.8 Mirror Velocity Errors 24
      4.4.9 Sampling Errors 24
      4.4.10 Optical Jitter-Induced Noise 25
      4.4.11 Total Noise-Equivalent Spectral Radiance 26

5. COMPARISON TO FILTER WHEEL RADIOMETER 29

APPENDIX A APODIZATION WITH A DETECTOR FIELD-OF-VIEW NOT ON THE OPTICAL AXIS 31

APPENDIX B PERMISSIBLE SURFACE ERRORS OF COMPONENTS 39

APPENDIX C MICHELSON INTERFEROMETER WITH RETROREFLECTOR MIRRORS 45
   C.1 Analysis of Retroreflector Displacement 47
   C.2 Approximate Expressions for the Fringe Modulation 52
   C.3 Retroreflectors *vs.* Plane Mirrors 55

REFERENCES 57

LIST OF ILLUSTRATIONS

Figure No.		Page
1	Optical diagram of a basic Michelson interferometer.	3
2	Fringe pattern evolution in the system focal plane, as the on-axis fringe phase varies through one cycle.	9
3	Geometry of detector acceptance field-of-view in the system focal plane.	10
A-1	The modulation factor for the GHIS spectrometer.	38
A-2	The residual phase error, in radians, for the GHIS spectrometer.	38
B-1	Typical layout of an unbalanced Michelson interferometer.	39
B-2	Geometry of rays refracted and externally reflected from a surface with a positive deviation S.	40
B-3	Geometry of rays refracted and internally reflected from a surface.	41
C-1	Michelson interferometer with corner-cube retroreflectors (schematic).	46
C-2	Close-up of a corner-cube retroreflector which has been displaced from its on-axis position by distance s.	46
C-3	Modulation factor $M(u, w)$, vs. retroreflector displacement, vs (in waves), for the case of FOV radius $\rho_0 = 1°$, and the interferometer OPD vx = 1,000 waves (u = 1.91).	51
C-4	Phase shift $\psi(u, w)$ vs. retroreflector displacement, vs (in waves), for the same case as in Figure C-3.	51

LIST OF SYMBOLS USED

A_d	detector area
A_o	area of the optical aperture
$A_o\Omega$	throughput, or *étendue*
β	azimuthal angle about the center of the field-of-view
b	ratio of electronic bandwidth to Nyquist frequency (≤ 1)
b_{eff}	effective number of bits of an analog-to-digital converter, allowing for non-linearity errors
B_v	spectral radiance
b_{nom}	nominal number of bits of an analog-to-digital converter
D^*	specific detectivity
f	temporal frequency
$F(v)$	[discrete] Fourier transform of interferogram
$f(x)$	interferogram (= $m(x)$)
f_{alias}	alias frequency
f_{Ny}	Nyquist frequency
f_{samp}	sampling frequency
$G(\alpha_0, \rho_0)$	geometrical factor in equation (14)
$H_i(v, x)$	integral of fringe amplitude, over Lyot stop
I_0	intensity at zero path difference (ZPD), i. e., $\Delta x = 0$.
I_d	detected intensity
L	maximum OPD
$M(\alpha_0, \rho_0)$, $M(e)$	modulation factor in the interferogram
$M(f)$	magnitude of electronic filter function [or overall transfer function]
$m(x)$	interferogram signal
N	total number of measurement samples of interferogram
n	index of refraction
n^2	noise power spectral density, referred to the input of the preamplifier

NEN	noise-equivalent spectral radiance
NEP	noise-equivalent power
N_s	number of spectral samples
P_1, P_2	partial terms in the expanded H integral
P_{sr}	spectral resolving power
$\mathcal{R}_n$	responsivity of the detector (in, e.g., Volts/Watt)
R	reflectance; radius of Lyot stop
(r,ϕ)	coordinates within Lyot stop
$S(r, \phi)$	surface irregularity
$s(x)$	total signal from the detector
S_ν	true spectral signal (see equation (5))
S'_ν	spectral signal from transform of interferogram (see equation (9))
SNR	signal-to-noise ratio
T	duration of the interferometer scan
T	transmission
V_{OPD}	optical path difference velocity (i.e., dx/dt)
α	angle from optical axis of interferometer; optical jitter amplitude
α_0	angular displacement of field-of-view from optical axis of interferometer
Δ	increase in optical path, caused by insertion of refracting plate
δ	local wavefront error, between the two interferometer beams; difference in optical paths; position error in sampling
Δf	electronic bandwidth
ΔM	change in modulation of interferogram, due to, e.g., optical jitter
$\delta\nu$	spectral resolution (unapodized, for Fourier Transform spectrometer)
Δt	difference in thickness of beamsplitter and compensator plates
Δx	optical path difference, or OPD
ε	angular misalignment within interferometer
ε_0	repeating portion of angular misalignment
ϕ	azimuthal angle about the interferometer optical axis

ϕ	optical phase difference; azimuthal angle of polar coordinates
η_s	beamsplitter efficiency
λ	wavelength
ν	wavenumber (usually measured in cm^{-1})
Π	symmetric, unit rectangular window function
θ	angle of incidence at the beamsplitter
Θ	region of integration representing the field-of-view
ρ	angle from center of field-of-view
ρ_0	angular radius of field-of-view
σ	root-mean-square noise amplitude
σ_{VEL}	rms variation in OPD velocity
τ	group delay time (of an electrical signal)
τ_{ox}	transmission of the optical system, excluding the beamsplitter
Ω	solid angle of field-of-view

1. INTRODUCTION

Weather satellites use infrared spectrometers to measure the temperature and humidity at various levels in the atmosphere, in a process known as *atmospheric sounding*. The sounder instrument of the newest Geostationary Operational Environmental Satellite, GOES-8, uses a filter wheel for this purpose. Lincoln Laboratory has undertaken a study of the feasibility of replacing the filter wheel on future GOES spacecraft with a Fourier Transform Spectrometer (FTS) [1],[2]. This report presents the theory of Fourier Transform Interferometry (FTI), as it relates to the proposed GOES High-Resolution Interferometer Sounder (GHIS). After a brief introduction, the basic theory is followed with a discussion of the performance limitations of the technique. Finally, the performance of the FTS is compared with that of a filter wheel system, using the same detectors and input optics.

Optical spectra were first measured with the use of an interferometer by Michelson in the nineteenth century. The utility of the technique was limited at the time, first by the lack of sufficiently quantitative detectors, and second by the difficulty of performing the necessary Fourier transforms. With the advent of electro-optical detectors, and especially digital computers, those barriers were removed by 1960. Fourier Transform Spectroscopy has since become a standard tool in the analytical laboratory. The Cooley-Tukey Fast Fourier Transform (FFT) algorithm (1965), and the exponential improvement in the cost/performance ratio of computer systems, have accelerated the trend.

Many Fourier Transform Spectrometer (FTS) instruments have been flown successfully in space, beginning in 1962. For a full review of those instruments, see the report by Mooney, et al. [3]. For a history of Fourier Transform Spectroscopy, and a detailed treatment of its principles, see *Introductory Fourier Transform Spectroscopy* by R. J. Bell [4]. The basic theory, and instrumental limitations, are also discussed by Brault [5].

2. PRINCIPLE OF OPERATION

The simplest type of FTS is based on a Michelson interferometer, as sketched in Figure 1. The incoming beam of collimated radiation is divided in two by the beamsplitter. The beam in each leg of the interferometer is reflected back toward the beamsplitter by a mirror. At the beamsplitter, each beam is again divided, one part going to the detector, the other returning to the input source. In each direction, the beams from the two legs recombine, or interfere. If the interferometer mirrors are correctly aligned, so that the wavefronts of the interfering beams are parallel, then the intensity of the light focused by the lens on the detector is modulated according to the optical phase difference of the beams from the two interferometer legs. The optical phase difference, ϕ, is given by $2\pi\Delta x/\lambda$, where λ is the wavelength of the light, and Δx is the optical path difference, or OPD. If y_1 and y_2 are the optical distances of the two interferometer mirrors from the beamsplitter, the OPD Δx equals $2(y_2 - y_1)$.

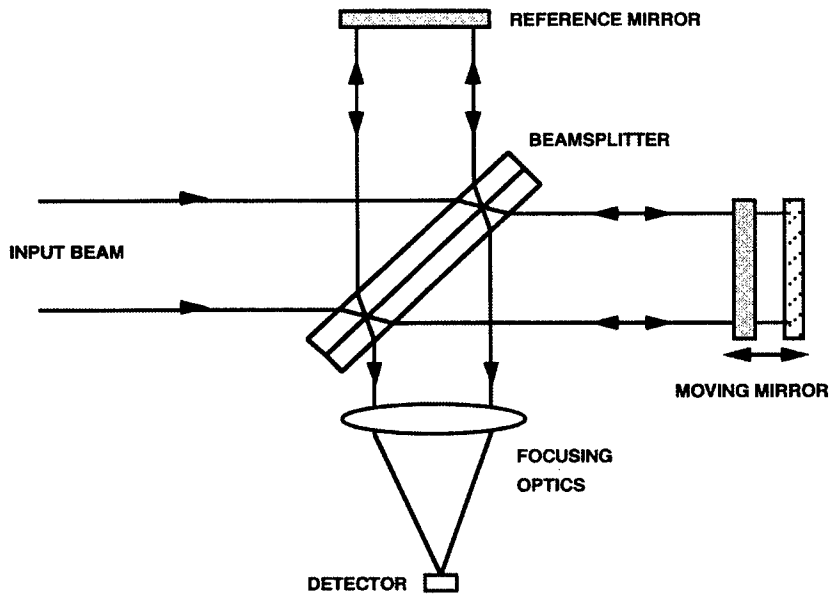

Figure 1. Optical diagram of a basic Michelson interferometer.

In operation, one or both of the interferometer mirrors are moved (while maintaining alignment) so Δx is varied. The intensity recorded at the detector, for a monochromatic source, is then given by

$$I_d(v,x) = \frac{1}{2} I_0[1 + cos(2\pi v \Delta x)] . \quad (1)$$

where

$\nu = 1/\lambda$, the wavenumber (usually measured in cm^{-1}),

I_0 = the intensity at zero path difference (ZPD), i.e., $\Delta x = 0$.

At the same time, the beams leaving by the input side of the interferometer interfere, with an intensity given by

$$I_i(\nu,x) = \frac{1}{2} I_0[1-\cos(2\pi\nu\Delta x)] \ . \tag{2}$$

Equation (2) is given here merely to show that energy is indeed conserved; the total power leaving the interferometer is constant, even though that at the detector is modulated. More complex instruments capture both outgoing beams, and subtract one interference signal from the other. However, such "balanced" designs are not considered in this report, since they require a second detector for each signal.

In the foregoing, it was assumed that both the reflectance, R, and transmission, T, of the beamsplitter were exactly one half. More generally, we find

$$I_d(\nu,x) = \frac{1}{2} I_0 \tau_{ox}\, \eta_s[1+\cos(2\pi\nu x)] \ , \tag{3}$$

where

$\eta_s = 4RT$ = the *beamsplitter efficiency*. (N. b.: $0 < \eta_s \leq 1$. $\eta_s = 1$ if $R = T = 0.5$),
τ_{ox} = the *transmission of the remainder of the optical system, excluding* the beamsplitter.

In the present application, the input is a spectral radiance, B_ν, composed of many wavenumbers, ν, the total signal from the detector, $s(x)$, becomes

$$s(x) = 2\int_0^\infty S_\nu[1+\cos(2\pi\nu x)]d\nu \ , \tag{4}$$

where we have defined a *spectral signal,* S_ν, as

$$S_\nu = \frac{1}{4} A_o \Omega \tau_{ox} \eta_s \Re_\nu B_\nu \ , \tag{5}$$

and

A_o = the area of the optical aperture,

Ω = the solid angle of accepted radiation, and

$\Re_\nu$ = the responsivity of the detector (in, e.g., Volts/Watt).

[N. b.: The product $A_o\Omega$, often called the *throughput*, or *étendue*, of the system, is an optical invariant. It is unchanged, from the input aperture to the detectors, as long as the optics are properly designed to avoid vignetting.]

The detector signal, equation (4), is composed of an unmodulated, or "DC" part, and a modulated, or "AC" part, of average value zero. The value of the unmodulated component is just equal to one half the signal at ZPD. The modulated component is called the *interferogram*. If we let the spectral signal be defined symmetrically for both positive and negative wavenumbers (i.e., $S_\nu(-\nu) = S_\nu(\nu)$), then the interferogram can be expressed* as

$$m(x) = \int_{-\infty}^{\infty} S_\nu \left[\cos(2\pi\nu x) + i\sin(2\pi\nu x)\right] d\nu \ , \text{or} \tag{6}$$

$$m(x) = \int_{-\infty}^{\infty} S_\nu e^{i2\pi\nu x} d\nu \ . \tag{7}$$

We see from equation (7) that $m(x)$ and S_ν form a *Fourier transform pair*. Hence, the spectral signal could be recovered from the interferogram as

$$S_\nu = \int_{-\infty}^{\infty} m(x) e^{-i2\pi\nu x} dx \ . \tag{8}$$

Full knowledge of the other factors in equation (5), many of which depend on wavenumber, then allows us to determine the spectral radiance, B_ν. The very important subject of radiometric calibration, however, is beyond the scope of the present report.

*The imaginary term in the integral is antisymmetric; hence it vanishes.

3. INHERENT LIMITATIONS

The preceding section presented the basic theory of the interferometer. Next, we describe some inherent limitations of the Michelson interferometer as a spectroscopic instrument.

3.1 RESOLUTION

The interferogram, $m(x)$, is what is directly measured by recording the detector output as a function of OPD. However, it obviously can not be determined for x from $-\infty$ to ∞! Instead, there is some *maximum OPD*, L. In this case, x is contained in $[-L, L]$, since we use a two-sided interferogram. We obtain an approximation to the spectral signal as

$$S'_\nu = \int_{-L}^{L} m(x) e^{-i2\pi\nu x} dx \quad . \tag{9}$$

This is equivalent to

$$S'_\nu = \int_{-\infty}^{\infty} \prod\left(\frac{x}{2L}\right) m(x) e^{-i2\pi\nu x} dx \quad , \tag{10}$$

where Π is the symmetric, unit rectangular window function. Since S'_ν is the transform of a *product* of two functions, then it is equal to the *convolution* of their (inverse) transforms. We have

$$S'_\nu = 2L\,\mathrm{sinc}(2L\nu) * S_\nu \quad \text{(the symbol * stands for convolution)}, \tag{11}$$

since the Fourier transform of $\Pi(x/2L)$ is given by

$$\mathsf{F}\left[\prod \frac{x}{2L}\right] = 2L\,\mathrm{sinc}(2L\nu) = \frac{\sin(2\pi L\nu)}{\pi\nu} \quad . \tag{12}$$

From equations (11) and (12), we find that the effect of the finite interferometer mirror stroke is to limit the *spectral resolution* of the computed spectrum. The true spectrum is convolved with an instrument resolution function, $\mathrm{sinc}(2L\nu)$, which has its first zero at

$$\delta\nu = \frac{1}{2L} \quad . \tag{13}$$

By convention, $\delta\nu$ is called the *unapodized spectral resolution* of the interferometer.

3.2 APODIZATION

So far, the incoming radiation has been treated as having a negligible angular divergence within the interferometer (i.e., $\Omega \approx 0$). All rays were assumed to be parallel to the interferometer optical axis, defined as the normal to the mirrors. For rays at an angle α to the axis, the interferometer operates in the same way, except that the OPD is no longer x, but rather $x\cos\alpha$. Returning to equation (4), the detector signal is now given by

$$s(x) = 2\int_0^\infty S_\nu \left\{ \frac{I}{\Omega} \iint_\Theta \left[1 + \cos(2\pi\nu x \cos\alpha)\right] \sin\alpha d\alpha d\phi \right\} d\nu \tag{14a}$$

or

$$s(x) = 2\int_0^\infty S_\nu \left[1 + G(\alpha_0, \rho_0)\right] d\nu \tag{14b}$$

where

ϕ = the azimuthal angle about the interferometer optical axis, and

Θ = the region of integration representing the acceptance field-of-view, of solid angle Ω.

and we have defined the geometrical, or monochromatic signal, factor in equations (14) as

$$G(\alpha_0, \rho_0) = \frac{1}{\Omega} \iint_\Theta \cos(2\pi\nu x \cos\alpha) \sin\alpha d\alpha d\phi \ . \tag{15}$$

The integrand in equations (14) represents an image in the field of view consisting of concentric circular fringes. They have an appearance similar to "Newton's rings," seen when a spherical optical surface is in close proximity to a planar one. The rings move in or out as x varies. Figure 2 shows a series of snapshots of the fringes, as νx ranges from 1000 to 1001 waves.

Assuming that the acceptance field-of-view is circular, as usual, but that it may be displaced from the interferometer optical axis, by an angle α_0, we can simplify the limits of integration by changing the angular variables to ρ, β, as defined in Figure 3.

Equation (15) may be written as

$$G(\alpha_0, \rho_0) = \frac{1}{\Omega} \int_{-\pi}^{\pi} \int_0^{\rho_0} \cos(2\pi\nu x \cos\alpha) \sin\rho d\rho d\beta \ , \tag{16}$$

and the solid angle of acceptance (included in the definition of S_ν) is given by

$$\Omega = \int_{-\pi}^{\pi} \int_0^{\rho_0} \sin\rho d\rho d\beta = 2\pi(1 - \cos\rho_0) \approx \pi\rho_0^2 \ . \tag{17}$$

In case $\alpha_0 = 0$, we have $\alpha = \rho$, and equation (16) becomes

$$G(0, \rho_0) = \frac{2\pi}{\Omega} \int_0^{\rho_0} \cos(2\pi\nu x \cos\rho) \sin\rho d\rho \ . \tag{18}$$

Making the substitution y = cosρ, this becomes

$$G(0, \rho_0) = \frac{2\pi}{\Omega} \int_{\cos\rho_0}^{1} \cos(2\pi\nu x y) dy \ , \tag{19}$$

from which

$$G(0, \rho_0) = \frac{1}{\nu x \Omega} \left[\sin(2\pi\nu x) - \sin(2\pi\nu x \cos\rho_0)\right] \ . \tag{20}$$

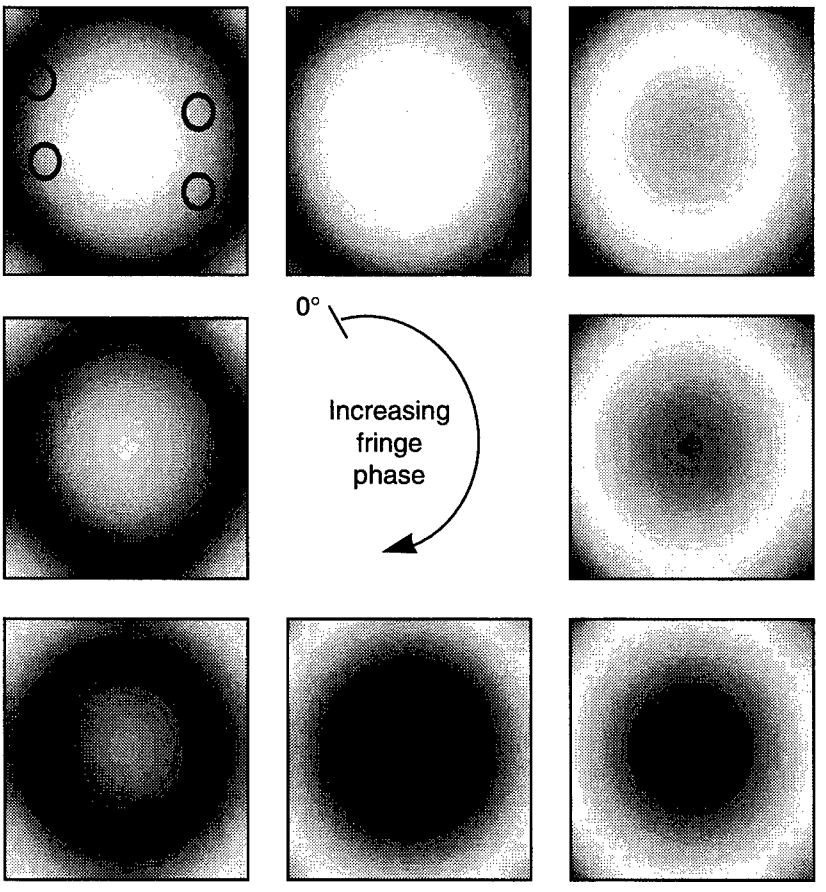

Figure 2. Fringe pattern evolution in the system focal plane, as the on-axis fringe phase varies through one cycle. The FOV shown is 30×30 mrad. The wavenumber is 2700 cm^{-1}, and the interferometer delay starts at 1000 waves on the axis.

Using equation (17), and the identity

$$\sin A - \sin B = 2\sin\left(\frac{A-B}{2}\right)\cos\left(\frac{A+B}{2}\right), \tag{21}$$

we arrive at

$$G(0,\rho_0) = \frac{2}{vx\Omega}\sin\left(\frac{vx\Omega}{2}\right)\cos\left(2\pi vx\left[1-\frac{\Omega}{4\pi}\right]\right). \tag{22}$$

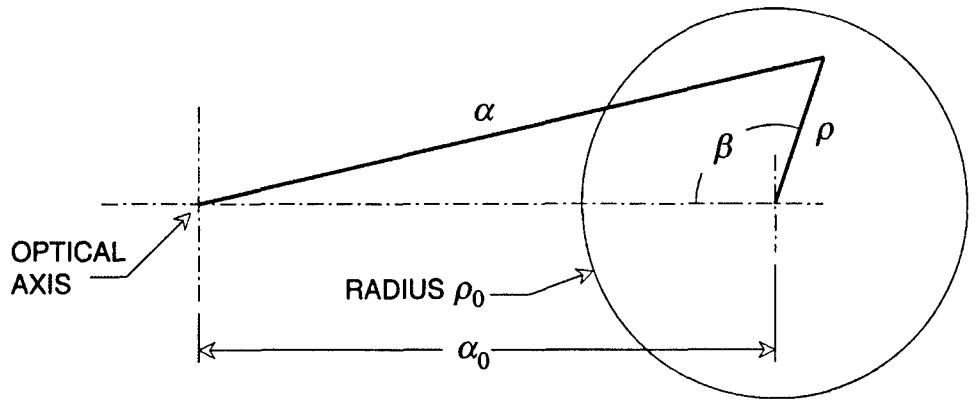

Figure 3. Geometry of detector acceptance field-of-view in the system focal plane. Each vector represents an angle in interferometer space.

If we use the definition of the sinc function,

$$\operatorname{sinc} x = \frac{\sin \pi x}{\pi x} , \tag{23}$$

equation (22) becomes

$$G(0,\rho_0) = \operatorname{sinc}\left(\frac{vx\Omega}{2\pi}\right)\cos\left(2\pi vx\left[1-\frac{\Omega}{4\pi}\right]\right) . \tag{24}$$

Thus, for the on-axis field stop, equation (14) becomes

$$s(x) = 2\int_0^\infty S_v\left[1+\operatorname{sinc}\left(\frac{vx\Omega}{2\pi}\right)\cos\left(2\pi vx\left[1-\frac{\Omega}{4\pi}\right]\right)\right]dv . \tag{25}$$

Comparison of equation (25) with equation (4) reveals the consequences of having a non-zero field-of-view, Ω. One effect is to shift the apparent wavenumber (or conversely, the apparent OPD), by a factor close to unity. The other effect is to *modulate* the fringe amplitude (or contrast) with a sinc function. The argument of the sinc function contains both the wavenumber and the OPD. The reduction of the fringe amplitude as |x| increases is often referred to as *self-apodization.*

The exact solution of the integration problem in the more general case, that $\alpha_0 \neq 0$, may be found in Appendix A, in terms of Lommel functions. Again, as a result of the non-zero aperture diameter, the interferogram is modulated by an overall factor, M, which reduces the fringe contrast as the OPD increases:

$$G(\alpha_0,\rho_0) \approx M(\alpha_0,\rho_0)\cos\left[2\pi vx\cos\alpha_0\left(1-\frac{\sin^2\rho_0}{4}\right)\right] \tag{A-34}$$

M is well approximated, for at least 1,000 waves of OPD, by

$$M(\alpha_0,\rho_0)\approx\left[1-\frac{(2\pi\nu x)^2\Omega}{8\pi}\left(\sin^2\alpha_0+\frac{\Omega}{12\pi}\right)\right] \quad . \tag{A-35b}$$

In addition to the fringe visibility reduction, the apparent wavenumber is altered, by a factor which depends on both the aperture size and its offset angle:

$$\nu'\approx\nu\cos\alpha_0\left(1-\frac{\Omega}{4\pi}\right) \quad . \tag{A-36}$$

By expanding the sinc function as a power series, the reader may easily verify that equation (A-34) reduces to the same solution as in equation (24), when α_0 goes to 0.

3.3 THROUGHPUT

The preceding section revealed that there is a trade-off to be made between optical throughput, $A_0\Omega$, and spectral resolution, $\delta\nu$. This comes about because of the solid angle factor in the apodization function in either equation (24) or equation (34). The modulation in the interferogram approaches zero as the product $\nu x\Omega$ approaches 2π. The maximum absolute value of x is L, which gives the spectral resolution (see equation (13)). Writing the sinc function in terms of spectral resolving power, P_{sr},

$$P_{sr}\equiv\frac{\nu}{\delta\nu} \quad ,$$

we have

$$\mathrm{sinc}\left(\frac{\nu L\Omega}{2\pi}\right)=\mathrm{sinc}\left(\frac{P_{sr}\Omega}{4\pi}\right) \quad . \tag{26}$$

Assuming that the application calls for a certain resolving power at a certain wavelength, one normally wishes to use the maximum solid angle to get the best signal-to-noise ratio. Since the interferogram signal (see equations (4) through (7)) also includes the solid angle factor, we wish to maximize the product

$$\Omega\,\mathrm{sinc}\left(\frac{P_{sr}\Omega}{4\pi}\right)=\frac{4}{P_{sr}}\sin\left(\frac{P_{sr}\Omega}{4}\right) \quad . \tag{27}$$

Staying within the central lobe of the sinc function, the maximum signal is obtained for

$$\Omega_{MAX}=\frac{2\pi}{P_{sr}} \quad . \tag{28}$$

Thus, there is an inverse relationship between the optical throughput, which is proportional to solid angle, and resolving power.

4. PRACTICAL LIMITATIONS

The preceding discussion concerned the theoretical capabilities of the Michelson interferometer. Next, we turn to the performance limitations of practical hardware, caused by the effects of optical misalignment, fabrication tolerances, and noise.

4.1 MISALIGNMENT

So far, we have implicitly assumed that the interferometer is perfectly aligned, that is to say, each mirror is exactly parallel to the image of the other mirror, formed by the beamsplitter. Suppose now that one mirror is misaligned by a small angle, ε. The optical path difference is now a function of the position of the rays within the aperture. Let the polar coordinates (r,ϕ) denote the position of the rays in the plane of the Lyot stop,* or aperture of the system. For these rays, the optical path difference, x, in our original expressions is replaced by

$$x' = x + 2\varepsilon r \sin\phi \quad . \tag{29}$$

The total signal, given by equation (4), now becomes

$$s(x) = 2\int_0^\infty S_v\left[1 + H_\varepsilon(v,x)\right]dv \quad , \tag{30}$$

where

$$H_\varepsilon(v,x) = \frac{1}{\pi R^2}\int_{-\pi}^{\pi}\int_0^R \cos\left[2\pi v\left(x + 2\varepsilon r\sin\phi\right)\right] r\,dr\,d\phi \quad , \text{ and} \tag{31}$$

R = the radius of the Lyot stop.

To evaluate H_ε, we first expand the cosine:

$$H_\varepsilon(v,x) = \frac{1}{\pi R^2}\left[P_1 - P_2\right] \quad , \tag{32}$$

where

$$P_1 = \cos(2\pi vx)\int_{-\pi}^{\pi}\int_0^R \cos\left(4\pi v\varepsilon r\sin\phi\right) r\,dr\,d\phi \quad , \text{ and} \tag{33}$$

$$P_2 = \sin(2\pi vx)\int_{-\pi}^{\pi}\int_0^R \sin\left(4\pi v\varepsilon r\sin\phi\right) r\,dr\,d\phi = 0 \quad . \tag{34}$$

Making use of the fact that [7]

$$\int_0^\pi \cos(x\sin\phi)d\phi = \pi J_0(x) \quad , \text{ and } \int x^n J_{n-1}(x)dx = x^n J_n(x)$$

*The Lyot stop is a defining aperture employed to minimize stray light reaching the detector. It was introduced in a solar coronagraph developed by B. Lyot in 1931. (See R. Klingslake, *Optical System Design* (1983), pp. 228-229 [6].) In an FTS, it is frequently located at the output of the interferometer.

leads to

$$H_\varepsilon(v,x)=\frac{2}{R^2}\cos(2\pi vx)\int_0^R J_0(4\pi v\varepsilon r)rdr \quad , \tag{35}$$

from which follows

$$H_\varepsilon(v,x)=\frac{2}{k}J_1(k)\cos(2\pi vx) \quad , \tag{36}$$

where

$$k\equiv 4\pi v\varepsilon R \quad , \tag{37}$$

We thus find that the interferogram is multiplied by a function of exactly the form found for diffraction from a circular aperture. For $k = 0$, its value is exactly 1. The first zero occurs for $k = 3.83$. For $k << 1$, we can use a power series expansion, retaining only the first two terms:

$$\frac{2}{k}J_1(k)=1-\frac{1}{2}\left(\frac{k}{2}\right)^2+\frac{1}{12}\left(\frac{k}{2}\right)^4-\cdots\approx 1-2(\pi v\varepsilon R)^2 \quad . \tag{38}$$

The condition $k << 1$ amounts to

$$\varepsilon << \frac{\lambda}{4\pi R} \quad , \tag{39}$$

which implies that the linear displacement of the mirror must vary by $<< \lambda/2\pi$ across its diameter. Otherwise, the fringe contrast will be significantly reduced.

In view of the sensitivity of the Michelson interferometer to tilt misalignment of the flat mirrors, one might use corner-cube retroreflector mirrors. However, retroreflectors also have a sensitivity. In their case, it is to translational alignment, as explained in Appendix C.

4.2 WAVEFRONT ERRORS

Michelson interferometers are quite sensitive to anything which causes a difference in the wavefronts of the two beams when they are recombined. This has just been shown for the case of misalignment. We now consider the effects of wavefront distortions, or optical path difference (OPD), caused by departures from flatness in the beamsplitter and interferometer mirror surfaces. In this treatment, the *nominal* OPD, x, caused by displacement of the moving mirror, will be referred to as the *optical delay*. The OPD from component distortions will be called *wavefront error*. This wavefront error is actually the *difference* between the wavefronts from the two interferometer arms, after recombination at the beamsplitter, and after removing the overall optical delay.

The analysis of wavefront errors begins almost exactly like that of misalignment (indeed, misalignment can be viewed as a special case of wavefront error):

$$s(x) = 2\int_0^\infty S_v\left[1 + H_\delta(v,x)\right]dv \quad , \tag{40}$$

where

$$H_\delta(v,x) = \frac{1}{\pi R^2}\int_{-\pi}^{\pi}\int_0^R \cos\left[2\pi v\left(x + \delta(r,\phi)\right)\right] r dr d\phi \quad , \tag{41}$$

R = the radius of the Lyot stop,

x = optical delay, between best-fit, flat wavefronts from the two arms, and

$\delta(r,\phi)$ = wavefront error at radius r, azimuth ϕ, in the Lyot stop.

Evaluation of the integral over the Lyot stop begins as in the case of tilt misalignment, starting with an expansion of the cosine:

$$H_\delta(v,x) = \frac{1}{\pi R^2}\left[P_1 - P_2\right] \quad , \tag{42}$$

where

$$P_1 = \cos(2\pi v x)\int_{-\pi}^{\pi}\int_0^R \cos\left(2\pi v\delta(r,\phi)\right) r dr d\phi \quad , \text{and} \tag{43a}$$

$$P_2 = \sin(2\pi v x)\int_{-\pi}^{\pi}\int_0^R \sin\left(2\pi v\delta(r,\phi)\right) r dr d\phi \quad . \tag{43b}$$

The quantity $v\delta(r,\phi)$ is the wavefront error, expressed in wavelengths, at wavenumber v. We know that this should be much less than one wave, in order to obtain an effective interferogram, so we use power series expansions of the cosine and sine:

$$\cos\left(2\pi v\delta(r,\phi)\right) = 1 - \frac{1}{2}\left(2\pi v\delta(r,\phi)\right)^2 + \cdots \quad , \text{and} \tag{44a}$$

$$\sin\left(2\pi v\delta(r,\phi)\right) = 2\pi v\delta(r,\phi) - \frac{1}{6}\left(2\pi v\delta(r,\phi)\right)^3 + \cdots \quad . \tag{44b}$$

We choose to define δ such that its mean value over the aperture is zero:

$$\int_{-\pi}^{\pi}\int_0^R \delta(r,\phi) r dr d\phi \equiv 0 \quad . \tag{45}$$

Also, we make the approximation that the third and higher powers of $v\delta$ average to zero over the Lyot stop. Making the substitutions in (43a), we have

$$P_1 \approx \cos(2\pi v x)\left[\pi R^2 - 2\pi^2\int_{-\pi}^{\pi}\int_0^R \left(v\delta(r,\phi)\right)^2 r dr d\phi\right] \quad , \text{or} \tag{46}$$

$$P_1 \approx \pi R^2 \cos(2\pi\nu x)\left[1 - 2\pi^2 \nu^2 \left\langle \delta^2 \right\rangle\right] \quad , \tag{47}$$

where

$\left\langle \delta^2 \right\rangle$ = the mean-squared value of the wavefront error.

Thus we find

$$H_\delta(\nu, x) \approx \cos(2\pi\nu x)\left[1 - 2\pi^2 \nu^2 \left\langle \delta^2 \right\rangle\right] \quad . \tag{48}$$

Once again, the interferogram contrast is now reduced by a modulation factor, given by

$$M_\delta \approx 1 - 2\pi^2 \nu^2 \left\langle \delta^2 \right\rangle \quad , \tag{49}$$

or more simply, the fringe contrast is reduced from its ideal value of one by

$$-\Delta M_\delta \approx 2\pi^2 \nu^2 \left\langle \delta^2 \right\rangle \quad , \tag{50}$$

The total wavefront error over the aperture is related to errors introduced by the various components (see Appendix B) as

$$\delta(r, \phi) = 2\left[S_{MS} - S_{MC} + \delta_{ST} - \delta_{CT} + 2S_3 \cos\theta\right] \quad , \tag{B-4}$$

where

$S_{MS}(r, \phi)$ = the surface irregularity of the mirror in the splitter arm,

$S_{MC}(r, \phi)$ = the surface irregularity of the mirror in the compensator arm,

$S_3(r, \phi)$ = the surface irregularity of the beam-splitting surface,

$\delta_{ST}(r, \phi)$ = the transmitted wavefront error of the beamsplitter,

$\delta_{CT}(r, \phi)$ = the transmitted wavefront error of the compensator, and

θ = the angle of incidence at the beamsplitter.

Appendix B gives further expressions which will be useful for estimating the loss of fringe contrast caused by specified tolerances on the surface irregularities and transmitted wavefront errors of the various optical components. Here, it is worthwhile to make two observations: First, irregularities of the splitting surface (S_3) cause roughly twice as much error as those on either mirror, because a negative deviation in one arm of the interferometer is subtracted from a positive deviation in the other. Second, *identical* irregularities on the two mirrors, or *identical* errors on the two transmissive parts, will cancel out.

4.3 SPLITTER-COMPENSATOR DIFFERENCES

A compensator plate was alluded to in the preceding subsection, but its function has not yet been explained. It is needed to balance the optical path length introduced by the plate (or substrate) on which the beam-splitting surface is formed. If the index of refraction of the splitter substrate were constant, no compensation would be needed, as the shift of one mirror would have the same effect. However, the phenomenon of dispersion in the substrate requires the addition of a compensator of exactly the same composition and thickness as the splitter substrate.

There must be some tolerance on the thicknesses of the beamsplitter and compensator plates, as actually fabricated. When a plate of thickness t is introduced into a beam at angle of incidence θ, the optical path is increased by

$$\Delta = t[n\cos\theta' - \cos\theta] = t\left[\sqrt{n^2 - \sin^2\theta} - \cos\theta\right] \quad . \tag{51}$$

The *difference* in optical paths, between the compensator and splitter plates, when their thicknesses differ by Δt, is

$$\delta = \Delta t\left[\sqrt{n^2 - \sin^2\theta} - \cos\theta\right] \quad . \tag{52}$$

The *change* in this OPD, between wavenumbers λ_1 and λ_2, where the indices of refraction are n_1 and n_2, respectively, is

$$\delta_\lambda = \Delta t\left[\sqrt{n_2^2 - \sin^2\theta} - \sqrt{n_1^2 - \sin^2\theta}\right] \quad . \tag{53}$$

This may be written as

$$\delta_\lambda = \Delta t\sqrt{n_1^2 - \sin^2\theta}\left[\sqrt{1 + \frac{\Delta n^2}{n_1^2 - \sin^2\theta}} - 1\right] \quad , \tag{54}$$

where we define

$$\Delta n^2 \equiv n_2^2 - n_1^2 \quad .$$

Assuming that $\Delta n << n$, the bracketed quantity in (54) may be expanded as a binomial series to yield the approximation

$$\delta_\lambda \approx \frac{\Delta t \Delta n^2}{2\sqrt{n_1^2 - \sin^2\theta}} \quad . \tag{55}$$

The beamsplitter and compensator for GHIS are to be made of KBr. The dispersion equation for the index of refraction of KBr at 22°C is (see [8], pp. 7-70*)

*Typographical errors in the formula as printed in the handbook are corrected in this report.

$$n^2 = 2.361323 - 3.11497\times10^{-4}\,\lambda^2 - 5.861\times10^{-8}\,\lambda^4 + \frac{7.676\times10^{-3}}{\lambda^2} + \frac{1.56569\times10^{-2}}{\lambda^2 - 0.0324}$$

where the wavelength is given in μm. In the wavelength range of GHIS (3.7 ~ 15 μm), we find that

$$\Delta n^2 \approx 3.11\times10^{-4}\left(\lambda_1^2 - \lambda_2^2\right) \quad .$$

With θ = 30° and λ_1 = 15 μm, we have

$$\delta_\lambda \approx 0.0245\left(1 - \left(\frac{\lambda_2}{15\mu m}\right)^2\right)\Delta t \quad .$$

The effect of the dispersive offset of the optical paths in the two interferometer arms is to introduce an asymmetry in the interferogram. The zero path difference position is truly zero only at one wavenumber; at other wavenumbers, it is shifted. When the Fourier transform is performed to obtain the raw spectrum (see equation (9)), an asymmetry will cause the appearance of an imaginary component in S_ν'. The raw spectrum will contain a complex phase factor, of phase $2\pi\nu\delta_\lambda$. The calibration process, carried out in either the interferogram or complex Fourier transform domains, should correct for this shift. However, as a guideline for system design, it is suggested that this phase angle be held to less than 2π, in order to prevent ambiguities in recovery of the phase.

4.4 NOISE SOURCES

The interferogram measurements from a real instrument will be affected by noise from many potential sources. First, we shall examine the relationship between the noise in the real interferogram and the resulting apparent noise in the computed spectrum. Then, the important sources of noise will be considered in turn.

4.4.1 Conversion from Interferogram to Spectral Domain

In practice, the interferogram is measured as a series of discrete samples, taken at N different points. As before, we assume a two-sided interferogram, so that $-L < x < L$, and the spacing between samples is thus

$$\delta x = \frac{2L}{N} \quad . \tag{56}$$

A *Discrete Fourier Transform* is performed on the interferogram, $f(x)$, which gives a computed spectrum, $F(\nu)$, also having N points. The spectrum $F(\nu)$ is periodic, with period $2\nu_n$. The following relations hold [5],[9]:

$$N = \frac{2L}{\delta x} = \frac{2\nu_n}{\delta\nu} = 2L\cdot 2\nu_n \quad . \tag{57}$$

We shall make use of the Rayleigh Power Theorem, which in discrete form is stated as

$$\delta x \sum_{m=0}^{N-1} f(x_m) f^*(x_m) = \delta v \sum_{j=0}^{N-1} F(v_j) F^*(v_j) \quad . \tag{58}$$

The theorem may also be restated as

$$2L\left\langle |f|^2 \right\rangle = 2v_n \left\langle |F|^2 \right\rangle \quad , \tag{59}$$

where the brackets denote the mean value over the whole period of the function.

In particular, suppose that in place of $f(x)$, we put a real measurement noise, σ_x, in the interferogram domain. We then have a direct relationship for the resulting noise in the spectral domain, σ_v:

$$\sigma_x \sqrt{2L} = \sigma_v \sqrt{2v_n} \quad . \tag{60}$$

From the relations (57) above, we find

$$\sigma_v = \frac{2L}{\sqrt{N}} \sigma_x \quad . \tag{61}$$

At this point, we make use of the fact that because the spectrum of incident light must be real, its true interferogram is *symmetric*. There is no such constraint on most sources of noise. Generally, the noise power in the interferogram will be evenly divided between symmetric and antisymmetric parts, which correspond to real and imaginary noise components, respectively, in the computed spectrum. The imaginary half of the noise *power* can be disregarded, so that the rms (root-mean-square) noise in the spectrum is divided by $\sqrt{2}$:

$$\sigma_v|_{REAL} = L\sqrt{\frac{2}{N}} \sigma_x \quad . \tag{62}$$

4.4.2 Noise-Equivalent Spectral Radiance

We specify the spectroradiometric performance of the instrument in terms of a *noise-equivalent spectral radiance*, denoted by NEN_v. This is just a radiance which would produce an output signal equivalent to the output noise, at each apparent wavenumber. If σ_v is the system spectral noise, then the noise-equivalent spectral radiance is given by

$$NEN_v = \frac{\sigma_v}{S_v} B_v \quad . \tag{63}$$

Substituting equation (5) for the signal, we have

$$NEN_v = \frac{4\sigma_v}{A_o \Omega \tau_{ox} \eta_s \mathcal{R}_v} \quad . \tag{64}$$

The system NEN_v is composed of contributions from various sources. Some of them are multiplicative, i.e., proportional to the input radiance. Most, however, are *additive* noise effects in the interferogram. Multiplicative noise sources, which include interferometer tilt jitter noise and velocity error noise, are evaluated as noise-to-signal ratios. The total of additive errors in the interferogram can be treated as the sum of the noise powers from the various individual sources:

$$\sigma_x^2 = \sum_i \sigma_{xi}^2 \quad , \{i\} = sources \ \ of \ \ noise. \tag{65}$$

Each term in the summation corresponds to a noise-equivalent spectral radiance contributed by that source:

$$NEV_v^2 = \sum_i NEN_{vi}^2 \quad . \tag{66}$$

We evaluate each noise contribution in terms of NEN_v in order to have a common basis for comparison of the different sources with each other, and of the system NEN_v with the required performance specification.

Upon expressing the spectral noise (equation (64)) in terms of the real noise in the interferogram (equation (62)), we find

$$NEN_v = \frac{4L\sigma_x}{A_o \Omega \tau_{ox} \eta_s \mathcal{R}_v} \sqrt{\frac{2}{N}} \quad . \tag{67}$$

4.4.3 Photon and Detector Noise

A very important class of additive noise appears at the output of the detector. It is made up of photon noise and detector noise. The photon noise (also called quantum noise) generally has a uniform, or "white" temporal spectrum, and it results from the inevitable statistical fluctuations in the number of photons converted to photoelectrons. (We assume that photon detectors are used here.) The detector noise can have several components. In semiconductor infrared detectors, charge carriers are generated by thermal excitation across the band gap. In photoconductive detectors, this is referred to as "thermal generation-recombination" noise, or "thermal G-R" noise. Photovoltaic detectors have a steady "dark current," which causes noise through its statistical fluctuations.

Both photon noise and intrinsic detector noise are usually lumped together and treated as the total "detector noise," which we shall designate $\sigma_{x,det}$. When divided by the detector responsivity, it gives the detector's *noise-equivalent power*:

$$NEP_{det} = \frac{\sigma_{x,det}}{\mathcal{R}_v} \quad . \tag{68}$$

The usual figure-of-merit for specifying detectors is the *specific detectivity*, or D^*. It is the reciprocal of the *NEP*, but normalized to unit detector area and temporal bandwidth:

$$D^* = \frac{\sqrt{A_d \Delta f}}{NEP_{det}} \quad , \tag{69}$$

where

A_d = the detector area, and

Δf = the electronic bandwidth.

(Notice that the conditions of the photon flux incident on the detector must be specified, along with D^*. In the present work, we calculate D^* based on the photon irradiance expected in use, and not on the more typical 295 K blackbody radiance over the full hemisphere.)

The effective noise bandwidth, Δf, in this sampled-data system is equal to the Nyquist frequency, which is one-half the sampling frequency:

$$\Delta f = f_{Ny} = \frac{1}{2} f_{samp} = \frac{N}{2T} \quad , \tag{70}$$

where

T = the duration of the interferometer scan, of N samples.

Returning to the expression for NEN_v in terms of interferogram noise (equation (67)), and using the foregoing definitions, we find a useful expression for the detector NEN_v:

$$NEN_{v,det} = \frac{4L}{A_o \Omega \tau_{ox} \eta_s D^*} \sqrt{\frac{A_d}{T}} \quad . \tag{71}$$

Using the definition of the unapodized spectral resolution, $\delta\nu$, this may also be written

$$NEN_{v,det} = \frac{2}{A_o \Omega \tau_{ox} \eta_s \delta\nu D^*} \sqrt{\frac{A_d}{T}} \quad . \tag{72}$$

4.4.4 Electronics Noise

The electronics following the detector also contributes noise. It mainly originates in the input stages of the preamplifier. It may be characterized by a noise power spectral density, n_{amp}, which is referred to the input of the preamplifier, i.e., the output terminal of the detector. It contributes an rms noise to the interferogram given by

$$\sigma_{x,amp} = n_{amp} \sqrt{\Delta f} = n_{amp} \sqrt{\frac{N}{2T}} \quad . \tag{73}$$

The NEN_v component contributed by electronics noise is thus

$$NEN_{v,amp} = \frac{4Ln_{amp}}{A_o \Omega \tau_{ox} \eta_s \Re_v \sqrt{T}} \quad . \tag{74}$$

4.4.5 Aliased Noise

When the discrete Fourier transform of a sampled signal is performed, only frequency components below the Nyquist limit are faithfully preserved. Any signal component beyond the Nyquist frequency appears in the spectrum at its *alias frequency*, given by

$$f_{alias} = f_{samp} - f = 2f_{Ny} - f \text{ (assuming that } f_{Ny} < f < 2f_{Ny}). \tag{75}$$

The raw signal must be filtered to eliminate components above the Nyquist frequency *before* sampling. Once they are sampled, such aliased components are inseparable from the true signal. Such filtering is done first in the optical domain, by passband filters and/or dichroic beamsplitters. Next, there is the spectral response characteristic of the detector. Finally, the electrical output of the detector is filtered. In the interferometer, the temporal frequency is directly related to the wavenumber by

$$f = v\frac{dx}{dt} = vV_{OPD} \quad , \tag{76}$$

where

V_{OPD} = the optical path difference velocity.

Heretofore, the *electronic filter* was assumed to have no effect on the signals being measured. In other words, its magnitude, $M(f)$, was taken as 1 exactly. To be correct, we must substitute $M(f)\Re_v$ wherever $\Re_v$ appears in the equations above.

Aliasing will produce a noise component corresponding to the combined detector and electronic rms noise amplitude times the electronic filter magnitude at the image frequency:

$$NEN_{v,alias} = M\left(f_{image}\right)\sqrt{NEN_{v,det}^2 + NEN_{v,amp}^2} \quad \text{, or} \tag{77}$$

$$NEN_{v,alias} = \frac{4LM\left(f_{image}\right)}{A_o \Omega \tau_{ox} \eta_s M\left(vV_{OPD}\right)} \sqrt{\frac{1}{T}\left[\frac{A_d}{D^{*2}} + \left(\frac{n_{amp}}{\Re_v}\right)^2\right]} \quad , \tag{78}$$

where

$$f_{image} = 2f_{Ny} - vV_{OPD} \quad . \tag{79}$$

4.4.6 Low-Frequency ("1/f") Noise

Semiconductor devices, including photoconductive IR detectors in particular, generally exhibit excess low-frequency noise. It is often called "$1/f$" noise, because its power spectral density has the form

$$\sigma_{1/f}^2 = Kf^{-a} \quad , \tag{80}$$

where a is a constant on the order of unity.

In device specifications, the magnitude of the $1/f$ noise is usually given in terms of the "white" noise, n_0, at higher frequencies, by specifying the "knee frequency," f_{knee}, at which the two components are equal. The total noise power takes the form

$$n^2 = n_0^2\left(1+\left(\frac{f_{knee}}{f}\right)^a\right) \quad . \tag{81}$$

The $1/f$ component of noise from the detector and amplifier can thus be included in the D^* and NEN_v expressions. Notice that the frequency dependence of these noise components now implies a wavenumber dependence in NEN_v (see equation (76)).

We saw earlier that electronic filtering is needed to attenuate high-frequency noise, so that it would not appear on the signal through aliasing. A high-pass filtering should be used as well, to attenuate the $1/f$ noise, at frequencies below the low-wavenumber end of the signal spectrum.

4.4.7 Quantization Noise

The analog-to-digital converter (ADC) introduces an rms error in the digitized signal, which is given by

$$\sigma_{x,ADC} = \frac{2\cdot m(0)}{2^{b_{eff}}\sqrt{12}} \quad , \tag{82}$$

where

$m(0)$ = the maximum anticipated interferogram signal, at the ZPD peak, and

$b_{eff} \approx b_{nom} - 1.5$ = the effective number of bits, accounting for ADC nonlinearity errors.

Referring to equations (5) and (7), we can write

$$m(0) = \frac{1}{4}A_o\Omega\int_{-\infty}^{\infty}\tau_{ox}\eta_s\mathcal{R}_v M\left(vV_{OPD}\right)B_v dv \quad . \tag{83}$$

The rms ADC error is thus

$$\sigma_{x,ADC} = \frac{A_o\Omega N\delta v}{2\cdot 2^{b_{eff}}\sqrt{12}}\left\langle\tau_{ox}\eta_s\mathcal{R}_v M\left(vV_{OPD}\right)B_v\right\rangle \quad , \tag{84}$$

where we have defined

$$\left\langle\tau_{ox}\eta_s\mathcal{R}_v M\left(vV_{OPD}\right)B_v\right\rangle \equiv \frac{2}{N\delta v}\int_0^{\infty}\tau_{ox}\eta_s\mathcal{R}_v M\left(vV_{OPD}\right)B_v dv \quad . \tag{85}$$

When $\sigma_{x,ADC}$ is substituted in the general NEN_ν expression (equation (67)), we find

$$NEN_{\nu,ADC} = \frac{1}{2^{b_{eff}}} \cdot \frac{\langle \tau_{ox}\eta_s \Re_\nu M(\nu V_{OPD}) B_\nu \rangle}{\tau_{ox}\eta_s \Re_\nu M(\nu V_{OPD})} \sqrt{\frac{N}{6}} \quad . \tag{86}$$

4.4.8 Mirror Velocity Errors

Ideally, the interferometer signal is sampled at uniform increments of optical path difference, Δx. To this end, a reference interferometer provides convenient position markers to trigger the sampling. The mirror velocity does not affect the measurement directly. However, the temporal frequency of the signals is proportional to the mirror velocity. Since the overall transfer function of the detector and electronics is, in general, not constant with frequency, a change of velocity will affect the measured amplitude and phase of any given spectral component.

We refer to the modulation in the *magnitude* of the spectral signals as *mirror velocity error.* It is characterized by a *Noise-to-Signal Ratio* (NSR) given by

$$NSR_{\nu,VEL} = \frac{\nu \sigma_{VEL}}{\sqrt{2}} \left| \frac{1}{M(f)} \frac{dM}{df} \right|_{f=\nu V_{OPD}} \quad , \tag{87}$$

where

σ_{VEL} = the rms variation in the OPD velocity, and

$M(f)$ = the magnitude of the overall transfer function at frequency f.

4.4.9 Sampling Errors

It is to be expected that the signals which trigger the sampling will contain some position error, whatever their source. An error in the position of the sample produces an error in the measured amplitude of the interferogram, which, for any given wavenumber, varies as the cosine of the OPD. The case of random (uncorrelated) sampling errors has been analyzed by Bell and Sanderson [10]. Expressed as a noise-equivalent radiance, the effect is

$$NEN_{SAMP} = 2\pi\delta \left[\nu B(\nu)\right]_{RMS} \quad , \tag{88}$$

where

$$\left(\left[\nu B(\nu)\right]_{RMS}\right)^2 \equiv \frac{1}{N\Delta\nu} \int_{\nu 1}^{\nu 2} \left[\nu B(\nu)\right]^2 d\nu \quad , \tag{89}$$

($\nu 1$, $\nu 2$) = the range of detectable wavenumbers, and

δ = the rms position error in the sampling.

The position error, δ, here includes error contributions from noise in the reference interferometer, and from electrical phase shifts induced by mirror velocity variations. The reference interferometer pulses will have an equivalent position error given by

$$\sigma_{x,REF} = \frac{\lambda_{REF}}{2\pi \cdot SNR_{REF}} \quad , \tag{90}$$

where

λ_{REF} = the reference wavelength, and

SNR_{REF} = the signal-to-noise ratio from the reference detector and amplifier.

Variations in the OPD velocity will shift the electrical frequency of the interferometer signals, as described earlier. This affects the phase, ϕ, of the electrical transfer function, as well as the magnitude. The group delay of the signal is

$$\tau = -\frac{1}{2\pi} \cdot \left. \frac{d\phi}{df} \right|_{f=vV_{OPD}} \quad . \tag{91}$$

Both the signal being measured and the reference signal have group delays, and it is the difference of these delays, times the random OPD velocity variation, which produces a random position error. When combined with the reference position error, we have, for the total sampling position error,

$$\delta = \sqrt{\left(\sigma_{VEL}\left(\tau_{IR} - \tau_{REF}\right)\right)^2 + \sigma_{x,REF}^2} \quad . \tag{92}$$

In the foregoing, the velocity variations were assumed to be random, i.e., uncorrelated from sample to sample. In practice, the velocity will probably vary slowly, on the time scale of the sampling. A narrow spectrum of velocity variations will result in relatively smaller sampling errors [11]. Thus, the expression given here for NEN_{SAMP} (equation (87)) may be regarded as an upper limit.

4.4.10 Optical Jitter-Induced Noise

In Section 4.1, it was shown that the amplitude of the interferogram is reduced by any misalignment of the interferometer. The modulation factor is

$$M(\varepsilon) = \frac{2}{k} J_1(k) \approx 1 - 2(\pi v \varepsilon R)^2 \quad , \tag{93}$$

where as before

ε = tilt error of interferometer mirror, and

R = radius of Lyot stop.

The tilt error, ε, will be composed of both a systematic, or repeatable tilt, ε_0, and a random tilt, α, also called *optical jitter*:

$$\varepsilon = \varepsilon_0 + \alpha \quad . \tag{94}$$

To find the modulation caused by the jitter alone, we perform a Taylor series expansion about the repeatable tilt position, ε_0:

$$\Delta M = -2(\pi v R)^2 \left[2\varepsilon_0 \alpha + \alpha^2 \right] \quad . \tag{95}$$

The variance of M is given by

$$\sigma_M^2 = \left\langle (\Delta M)^2 \right\rangle - \langle \Delta M \rangle^2 \quad . \tag{96}$$

In terms of the variance and mean of the tilt components, this is

$$\sigma_M^2 = 4(\pi v R)^4 \left[4\left\langle \varepsilon_0^2 \right\rangle \sigma_\alpha^2 + 2\sigma_\alpha^4 \right] \quad , \tag{97}$$

where

$$\langle \alpha \rangle = 0 \quad \sigma_\alpha^2 \equiv \left\langle \alpha^2 \right\rangle \quad .$$

The modulation caused by the jitter results in a multiplicative noise in the spectrum, given by

$$NSR_{JITT} = \frac{\sigma_M}{\sqrt{2}} = 2(\pi v R)^2 \sigma_\alpha \sqrt{2\left\langle \varepsilon_0^2 \right\rangle + \sigma_\alpha^2} \quad . \tag{98}$$

The square root of two reduction in the noise comes from the fact that only the *real* noise power, and not the imaginary component, contributes to noise in the reconstructed spectrum, for the case of two-sided interferograms.

4.4.11 Total Noise-Equivalent Spectral Radiance

To summarize the foregoing results, the total noise-equivalent spectral radiance is given by

$$NEN_v^2 = \sum_i NEN_i^2 + B_v^2 \sum_j NSR_j^2 \quad , \tag{99}$$

where the additive noise components are

$$NEN_{v,det} = \frac{4L}{A_o \Omega \tau_{ox} \eta_s D^*} \sqrt{\frac{A_d}{T}} \quad \text{from the detector,} \tag{71}$$

$$NEN_{v,amp} = \frac{4Ln_{amp}}{A_o \Omega \tau_{ox} \eta_s \mathcal{R}_v \sqrt{T}} \quad \text{from the amplifier,} \tag{74}$$

$$NEN_{v,alias} = M\left(f_{image}\right) \sqrt{NEN_{v,det}^2 + NEN_{v,amp}^2} \quad \text{from aliasing,} \tag{77}$$

$$NEN_{v,ADC} = \frac{1}{2^{b_{eff}}} \cdot \frac{\langle \tau_{ox}\eta_s \Re_v M(vV_{OPD}) B_v \rangle}{\tau_{ox}\eta_s \Re_v M(vV_{OPD})} \sqrt{\frac{N}{6}} \quad \text{from quantization, and} \tag{86}$$

$$NEN_{SAMP} = 2\pi\delta\left[vB(v)\right]_{RMS} \quad \text{from sampling errors.} \tag{88}$$

The multiplicative noise components are

$$NEN_{v,VEL} = \frac{v\sigma_{VEL}}{\sqrt{2}} \left| \frac{1}{M(f)} \frac{dM}{df} \right|_{f=vV_{OPD}} \quad \text{from velocity variations,} \tag{87}$$

and from optical jitter within the interferometer,

$$NSR_{JITT} = \frac{\sigma_M}{\sqrt{2}} = 2(\pi v R)^2 \sigma_\alpha \sqrt{2\langle \varepsilon_0^2 \rangle + \sigma_\alpha^2} \quad . \tag{98}$$

Refer to the preceding subsections for a full description of the variables occurring in these expressions.

5. COMPARISON TO FILTER WHEEL RADIOMETER

It may be instructive to compare the noise-equivalent spectral radiance of the FTS to that of a filter wheel radiometer having the same overall system parameters [12]. For a filter wheel radiometer, the signal is

$$S_v = A_o \Omega \tau_{ox} \delta v \mathcal{R}_v B_v \quad , \tag{100}$$

while the noise, assumed to come from the detector, is

$$\sigma_v = NEP_{det} \mathcal{R}_v = \frac{\mathcal{R}_v \sqrt{A_d \Delta f}}{D^*} \quad . \tag{101}$$

The noise-equivalent spectral radiance is thus

$$NEN_{v,FWR} = \frac{\sqrt{A_d \Delta f}}{A_o \Omega \tau_{ox} \delta v D^*} \quad . \tag{102}$$

The measurement bandwidth, Δf, is inversely proportional to the integration time for each measurement

$$\Delta f = \frac{1}{2t_i} \quad . \tag{103}$$

Assuming equal dwell times on each wavenumber, the integration time is given by

$$t_i \leq \frac{\delta v}{v_2 - v_1} T \quad , \tag{104}$$

where an inequality is shown, because some of the total measurement time, T, should be spent in sampling the background level. (All variables used here have the same definitions as for the interferometer.)

The noise-equivalent spectral radiance for the filter wheel radiometer reduces to

$$NEN_{v,FWR} \geq \frac{1}{A_o \Omega \tau_{ox} \delta v D^*} \sqrt{\frac{A_d (v_2 - v_1)}{2 \delta v T}} \quad . \tag{105}$$

For the Fourier Transform Spectrometer, we also assume that detector noise is the dominant term, as is generally the case. It is given by

$$NEN_{v,det,FTS} = \frac{4L \sqrt{A_d \Delta f}}{A_o \Omega \tau_{ox} \eta_s D^*} \sqrt{\frac{2}{N}} \quad . \tag{106}$$

For the FTS, the noise bandwidth is equal to the Nyquist frequency:

$$\Delta f = \frac{N}{2T} \quad , \tag{107}$$

hence

$$NEN_{v,FTS} = \frac{2}{A_o \Omega \tau_{ox} \eta_s \delta v D^*} \sqrt{\frac{A_d}{T}} \quad . \tag{108} \approx (72)$$

When we take the ratio of the noise levels for the two instruments, we find

$$\frac{NEN_{v,FTS}}{NEN_{v,FWR}} \leq \frac{2D^*_{FWR}}{\eta_s D^*_{FTS}} \sqrt{\frac{2\delta v}{(v_2 - v_1)}} \quad . \tag{109}$$

Here we have retained the D* factors for the two separate instruments. If the D*'s in both cases are dominated by thermal (i.e., internal) noise sources, they would be equal and would cancel each other in equation (109). In that case we have, assuming that the beamsplitter efficiency is roughly 100%,

$$\left.\frac{NEN_{v,FTS}}{NEN_{v,FWR}}\right|_{Det.Limit} \leq \sqrt{\frac{8}{N_s}} \quad , \tag{110}$$

where N_s is the number of spectral samples, assumed to be the same for both instruments. This expression shows the *multiplex advantage* ascribed to Fourier transform spectrometers.

At the other extreme, the detector D^*'s could be dominated by signal photon noise in both cases. Then we have

$$D^*_{FTS} \propto \frac{1}{\sqrt{(v_2 - v_1)\bar{B}_v}} \quad , \text{ and } \quad D^*_{FWR} \propto \frac{1}{\sqrt{\delta v B_v}} \quad , \tag{111a, b}$$

where $\bar{B}_v$ is the *average* spectral radiance over the spectral passband, (v_1, v_2). The ratio of the system noises becomes

$$\left.\frac{NEN_{v,FTS}}{NEN_{v,FWR}}\right|_{Photon.Limit} \leq \sqrt{\frac{8\bar{B}_v}{B_v}} \quad . \tag{112}$$

In this case, the Fourier transform spectrometer has a multiplex *disadvantage*, because each spectral sample is affected by photon noise from the entire passband. In addition, there is the loss of 50% of the incident energy out the input port of the interferometer. Equation (112) still shows the FTS to be superior for measuring a few strong emission lines. Conversely, the FTS would be particularly poor at delineating narrow absorption features in a spectrum.

APPENDIX A

APODIZATION WITH A DETECTOR FIELD-OF-VIEW NOT ON THE OPTICAL AXIS

The topic of self-apodization in an interferometer by an extended field-of-view was introduced in Section 2. The geometry of the field angles is shown in Figure 3, which is repeated here for convenience. The simple case, in which the circular field-of-view is centered on the optical axis (i.e., $\alpha_0 = 0$), is treated in Section 2. Here we treat the more general case of $\alpha_0 \neq 0$.

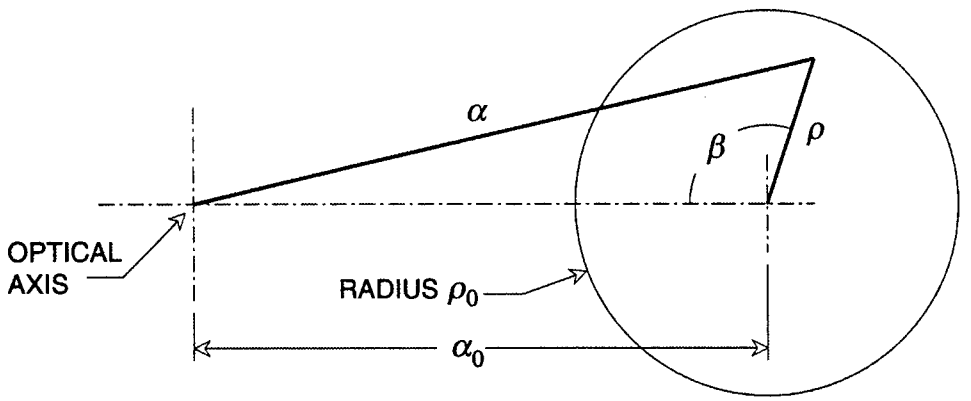

Figure 3. Geometry of detector acceptance field-of-view in the system focal plane. Each vector represents an angle in interferometer space.

The starting points of the analysis are the following equations:

$$s(x) = 2\int_0^\infty S_\nu\left[1 + G(\alpha_0, \rho_0)\right]d\nu \tag{14b}$$

for the detected signal, where

$$G(\alpha_0, \rho_0) = \frac{1}{\Omega}\int_{-\pi}^{\pi}\int_0^{\rho_0} \cos(2\pi\nu x \cos\alpha)\sin\rho d\rho d\beta \ , \tag{16}$$

and the solid angle of acceptance (included in the definition of S_ν) is given by

$$\Omega = \int_{-\pi}^{\pi}\int_0^{\rho_0} \sin\rho d\rho d\beta = 2\pi(1 - \cos\rho_0) \approx \pi\rho_0^2 \ . \tag{17}$$

The spherical law of cosines gives

$$\cos\alpha = \cos\alpha_0 \cos\rho + \sin\alpha_0 \sin\rho\cos\beta \ . \tag{A-1}$$

When this is applied to the G integral, we obtain

$$G(\alpha_0,\rho_0) = \frac{1}{\Omega}\int_{-\pi}^{\pi}\int_0^{\rho_0} \cos[C\cos\rho + S\sin\rho\cos\beta]\sin\rho d\rho d\beta \ . \tag{A-2}$$

where we have defined

$$C \equiv 2\pi v x \cos\alpha_0 \quad \text{and} \quad S \equiv 2\pi v x \sin\alpha_0 \ . \tag{A-3a, b}$$

Expanding the argument of the cosine in brackets [...], G may be written

$$G(\alpha_0\rho_0) = \frac{1}{\Omega}(Q_1 - Q_2) \tag{A-4}$$

$$Q_1 = \int_{-\pi}^{\pi}\int_0^{\rho_0} \cos[C\cos\rho]\cos[S\sin\rho\cos\beta]\sin\rho d\rho d\beta \tag{A-5a}$$

$$Q_2 = \int_{-\pi}^{\pi}\int_0^{\rho_0} \sin[C\cos\rho]\sin[S\sin\rho\cos\beta]\sin\rho d\rho d\beta \tag{A-5b}$$

We observe that in equation (A-5b), the integrand is antisymmetric in β, so $Q_2 = 0$. The integration over β for Q_1 yields

$$Q_1 = 2\pi\int_0^{\rho_0} \cos[C\cos\rho]J_0(S\sin\rho)\sin\rho d\rho \,, \tag{A-6}$$

where use has been made of [7]

$$\int_0^{\pi}\cos(x\cos\phi)d\phi = \pi J_0(x) \ .$$

In order to evaluate the integral in equation (A-6), we substitute

$$r = \frac{\sin\rho}{\sin\rho_0}, \quad dr = \frac{\cos\rho}{\sin\rho_0}d\rho, \quad \cos\rho = \sqrt{1 - r^2\sin^2\rho_0} \ ,$$

which leads to

$$Q_1 = 2\pi\sin^2\rho_0\int_0^1 \cos\left[C\sqrt{1-r^2\sin^2\rho_0}\right]J_0(Sr\sin\rho_0)\frac{r}{\sqrt{1-r^2\sin^2\rho_0}}dr \ . \tag{A-7}$$

We introduce the approximations

$$\sqrt{1-r^2\sin^2\rho_0} \approx 1-\frac{1}{2}r^2\sin^2\rho_0 \tag{A-8a}$$

and

$$\frac{1}{\sqrt{1-r^2\sin^2\rho_0}} \approx 1+\frac{1}{2}r^2\sin^2\rho_0 \quad , \tag{A-8b}$$

and neglect $\sin^2\rho_0$ relative to 1 in the overall factor (A-8b). We also make use of

$$\Omega = 2\pi(1-\cos\rho_0) = 4\pi\sin^2\frac{\rho_0}{2} \quad , \tag{A-9a}$$

and

$$\pi\sin^2\rho_0 = 4\pi\sin^2\frac{\rho_0}{2}\cos^2\frac{\rho_0}{2} = \Omega\left(1-\sin^2\frac{\rho_0}{2}\right) \approx \Omega \quad . \tag{A-9b}$$

When the cosine factor in (A-7) is expanded, and the relationships (A-8) and (A-9) are applied, we find

$$Q_1 \approx \Omega\left[A(C,S)\cos C + B(C,S)\sin C\right] \tag{A-10}$$

or, using (A-4) and remembering that $Q_2 = 0$,

$$G(\alpha_0,\rho_0) \approx \left[A(C,S)\cos C + B(C,S)\sin C\right] \quad , \tag{A-11}$$

where

$$A(C,S) = 2\int_0^1 J_0(Sr\sin\rho_0)\cos\left(\frac{1}{2}Cr^2\sin^2\rho_0\right)rdr \quad , \text{ and} \tag{A-12a}$$

$$B(C,S) = 2\int_0^1 J_0(Sr\sin\rho_0)\sin\left(\frac{1}{2}Cr^2\sin^2\rho_0\right)rdr \quad . \tag{A-12b}$$

Evaluation of the two r integrals in equations (A-12) yields a solution in terms of *Lommel functions* (see [13], Sec. 8.8.1, pp. 435-439). The Lommel functions are defined as

$$U_n(u,w) = \sum_{s=0}^{\infty}(-1)^s\left(\frac{u}{w}\right)^{n+2s}J_{n+2s}(w) \quad , \text{ and} \tag{A-13a}$$

$$V_n(u,w) = \sum_{s=0}^{\infty}(-1)^s\left(\frac{w}{u}\right)^{n+2s}J_{n+2s}(w) \quad . \tag{A-13b}$$

The integrals for A and B are found to be

$$A(C,S)=\frac{\cos\frac{1}{2}u}{\frac{1}{2}u}U_1(u,w)+\frac{\sin\frac{1}{2}u}{\frac{1}{2}u}U_2(u,w) \quad , \text{ and} \tag{A-14a}$$

$$B(C,S)=\frac{\sin\frac{1}{2}u}{\frac{1}{2}u}U_1(u,w)-\frac{\cos\frac{1}{2}u}{\frac{1}{2}u}U_2(u,w) \quad , \tag{A-14b}$$

where u and w are defined as

$$u\equiv C\sin^2\rho_0 \quad , \quad w\equiv S\sin\rho_0 \quad . \tag{A-15a,b}$$

We also use

$$\frac{u}{w}=\frac{C}{S}\sin\rho_0=\frac{\cos\alpha_0\sin\rho_0}{\sin\alpha_0}\approx\frac{\rho_0}{\alpha_0} \quad . \tag{A-16}$$

Equations (A-14) can also be written as

$$A(C,S)=M(C,S)\left[\cos\frac{1}{2}u\cos\psi+\sin\frac{1}{2}u\sin\psi\right]=M(C,S)\cos\left(\frac{1}{2}u-\psi\right) \quad , \tag{A-17a}$$

and

$$B(C,S)=M(C,S)\left[\sin\frac{1}{2}u\cos\psi-\cos\frac{1}{2}u\sin\psi\right]=M(C,S)\sin\left(\frac{1}{2}u-\psi\right) \quad , \tag{A-17b}$$

where we define

$$M(C,S)\cos\psi=\frac{2}{u}U_1(u,w) \quad , \quad M(C,S)\sin\psi=\frac{2}{u}U_2(u,w) \quad , \tag{A-18a,b}$$

and

$$\tan\psi=\frac{U_2(u,w)}{U_1(u,w)} \quad . \tag{A-19}$$

We observe that

$$M(C,S)=\frac{2}{u}\sqrt{\left(U_1(u,w)\right)^2+\left(U_2(u,w)\right)^2} \quad . \tag{A-20}$$

Equation (A-11) now becomes, for the monochromatic signal factor in equation (14),

$$G(\alpha_0,\rho_0)=M(C,S)\left[\cos\left(\frac{1}{2}u-\psi\right)\cos C+\sin\left(\frac{1}{2}u-\psi\right)\sin C\right] \quad , \text{ or} \tag{A-21}$$

$$G(\alpha_0,\rho_0) = M(C,S)\cos\left(C - \frac{1}{2}u + \psi\right) \quad . \tag{A-22}$$

The factor $M(C,S)$ given in equation (A-22) is now seen to be a *modulation factor*, which changes the apparent amplitude of the interferogram. The *phase* of the interferogram is also modified by the quantity $u/2 - \psi$.

While equation (A-22) represents an analytical solution to the problem of an off-axis field-of-view, the behavior of the unusual functions it contains is far from obvious. We need to examine its various components, using reasonable value ranges for the constant parameters. First, we observe from equation (A-16) that $u/w \approx \rho_0/\alpha_0$, which, for GHIS, is much less than one. (Therefore, the U_n solution was chosen over the V_n.) As for w, the argument of the Bessel functions in (A-13), we have

$$w \equiv S\sin\rho_0 = 2\pi\nu x \sin\alpha_0 \sin\rho_0 \quad ,$$

and both ρ_0 and α_0 are usually small. (GHIS: ρ_0 = 4.48 mrad, $\alpha_{0,\mathrm{MAX}}$ = 25.9 mrad.) On the other hand, νx is the optical delay expressed in wavelengths, and is related to the relative wavenumber resolution (often simply called "resolution" by spectroscopists) as

$$|\nu x| \le \nu L = \frac{1}{2}\left(\frac{\nu}{\delta\nu}\right) \quad .$$

For GHIS again, νx is less than 1,000, but other applications could require higher resolution. The maximum value of w for GHIS is 0.671 (ν = 1150 cm^{-1}, x = 0.8 cm).

With this regime of values in mind, let us examine the Lommel functions. From (A-13a), we have

$$U_1(u,w) = \left(\frac{u}{w}\right)\left[J_1(w) - \left(\frac{u}{w}\right)^2 J_3(w) + \left(\frac{u}{w}\right)^4 J_5(w) - \cdots\right] \quad , \tag{A-23}$$

or

$$U_1(u,w) = \left(\frac{u}{w}\right)J_1(w)\left[1 - \left(\frac{u}{w}\right)^2 \frac{J_3(w)}{J_1(w)} + \left(\frac{u}{w}\right)^4 \frac{J_5(w)}{J_1(w)} - \cdots\right] \quad . \tag{A-24}$$

Making use of the identity

$$2nJ_n(w) = wJ_{n-1}(w) + wJ_{n+1}(w) \quad , \tag{A-25}$$

we find (after considerable algebraic manipulation)

$$U_2(u,w) = \frac{u}{4}\left(\frac{u}{w}\right)J_1(w)\left[1 + \left\{1 - \frac{1}{2}\left(\frac{u}{w}\right)^2\right\}\frac{J_3(w)}{J_1(w)} + \left\{\frac{1}{2} - \frac{1}{3}\left(\frac{u}{w}\right)^2\right\}\left(\frac{u}{w}\right)^2 \frac{J_5(w)}{J_1(w)} - \cdots\right] \quad . \tag{A-26}$$

In this regime, the Bessel functions are well approximated by the first terms in their power series expansions:

$$J_n(w)=\left(\frac{w}{2}\right)^n\sum_{k=0}^{\infty}\frac{(-1)^k}{k!(n+k)!}\left(\frac{w}{2}\right)^{2k}\approx\frac{1}{n!}\left(\frac{w}{2}\right)^n \quad . \tag{A-27}$$

Thus, we have

$$\frac{J_3(w)}{J_1(w)}\approx\frac{1}{3!}\left(\frac{w}{2}\right)^2 \quad , \quad \frac{J_5(w)}{J_1(w)}\approx\frac{1}{5!}\left(\frac{w}{2}\right)^4 \quad , \text{ etc.}$$

U_1 and U_2 can now be written

$$U_1(u,w)\approx\left(\frac{u}{w}\right)J_1(w)\left[1-\frac{1}{6}\left(\frac{u}{2}\right)^2+\frac{1}{120}\left(\frac{u}{2}\right)^4-\cdots\right] \quad , \tag{A-28}$$

and

$$U_2(u,w)\approx\frac{u}{4}\left(\frac{u}{w}\right)J_1(w)\left[1+\frac{1}{6}\left\{\left(\frac{w}{2}\right)^2-\frac{1}{2}\left(\frac{u}{2}\right)^2\right\}+\frac{1}{120}\left\{\frac{1}{2}\left(\frac{w}{2}\right)^2-\frac{1}{3}\left(\frac{u}{2}\right)^2\right\}\left(\frac{u}{2}\right)^2+\cdots\right] . \tag{A-29}$$

When the foregoing expressions are inserted in equation (A-20), and the terms higher than second order are dropped, we find

$$M(C,S)\approx\frac{2}{w}J_1(w)\sqrt{1-\frac{1}{3}\left(\frac{u}{2}\right)^2+\left(\frac{u}{4}\right)^2\left[1+\frac{1}{6}\left(\frac{w}{2}\right)^2\right]} \quad , \tag{A-30}$$

or more simply,

$$M(C,S)\approx\frac{2}{w}J_1(w)\sqrt{1-\frac{u^2}{48}} \quad . \tag{A-31}$$

Applying the power series for the Bessel function (to second order), this becomes

$$M(C,S)\approx\left(1-\frac{w^2}{8}\right)\left(1-\frac{u^2}{96}\right)\approx1-\frac{w^2}{8}-\frac{u^2}{96} \quad . \tag{A-32}$$

We also need the phase angle, ψ, from the definition (A-19). Inserting the approximate expressions (A-28) and (A-29), and applying a binomial expansion for the denominator, we find

$$\tan\psi\approx\frac{u}{4}\left[1+\frac{1}{6}\left(\frac{w}{2}\right)^2-\frac{1}{12}\left(\frac{u}{2}\right)^2\right]\cdot\left[1+\frac{1}{6}\left(\frac{u}{2}\right)^2\right]\approx\frac{u}{4}\left[1+\frac{w^2}{24}+\frac{u^2}{48}\right] \quad . \tag{A-33}$$

Equation (A-22), which describes the fringe amplitude, finally becomes (with $\tan\psi\approx\psi$), after inserting the definitions of u, w, C, and S,

$$G(\alpha_0,\rho_0) \approx M(\alpha_0,\rho_0)\cos\left[2\pi\nu x\cos\alpha_0\left(1-\frac{\sin^2\rho_0}{4}\right)\right] \quad , \tag{A-34}$$

where

$$M(\alpha_0,\rho_0) \approx \left[1-\frac{(2\pi\nu x)^2\sin^2\rho_0}{8}\left(\sin^2\alpha_0+\frac{\cos^2\alpha_0\sin^2\rho_0}{12}\right)\right] \quad . \tag{A-35a}$$

or, using (A-9b) and $\cos\alpha_0 \approx 1$,

$$M(\alpha_0,\rho_0) \approx \left[1-\frac{(2\pi\nu x)^2\Omega}{8\pi}\left(\sin^2\alpha_0+\frac{\Omega}{12\pi}\right)\right] \quad . \tag{A-35b}$$

We observe from equation (A-34) that the effective wavenumber in the interferogram has become (using (A-9b))

$$\nu' \approx \nu\cos\alpha_0\left(1-\frac{\Omega}{4\pi}\right) \quad . \tag{A-36}$$

The foregoing approximate expressions were derived in order to elucidate the basic behavior of the modulation, M, and the phase factor in the interferogram (see equations (14b) and (A-22)). In practice, it is not difficult to evaluate the actual functions, with, for example, a good spreadsheet program. This has been done in WingZ on the Macintosh, for the particular angles of the aperture radius and offset of the GHIS spectrometer (α_0 = 25.9 mrad, ρ_0 = 4.48 mrad, in interferometer space). The behavior of the modulation factor $M(\alpha_0, \rho_0)$ is plotted in Figure A-1. For the same system, the residual phase error in radians, after using the effective wavenumber given in (A-36), is shown in Figure A-2.

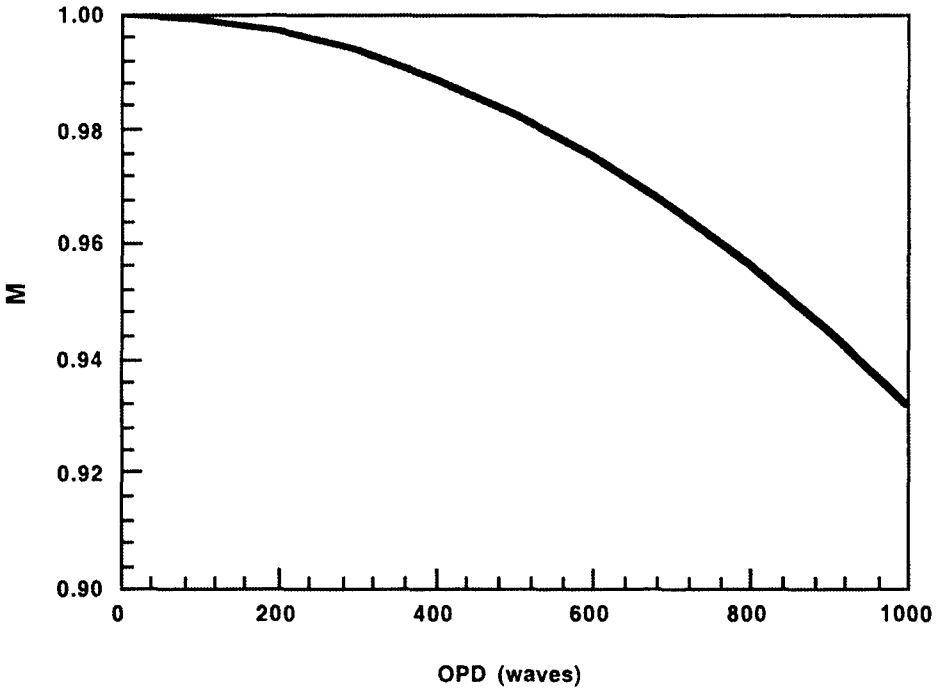

Figure A-1. The modulation factor for the GHIS spectrometer, caused by the offset and radius of the detector aperture (field stop).

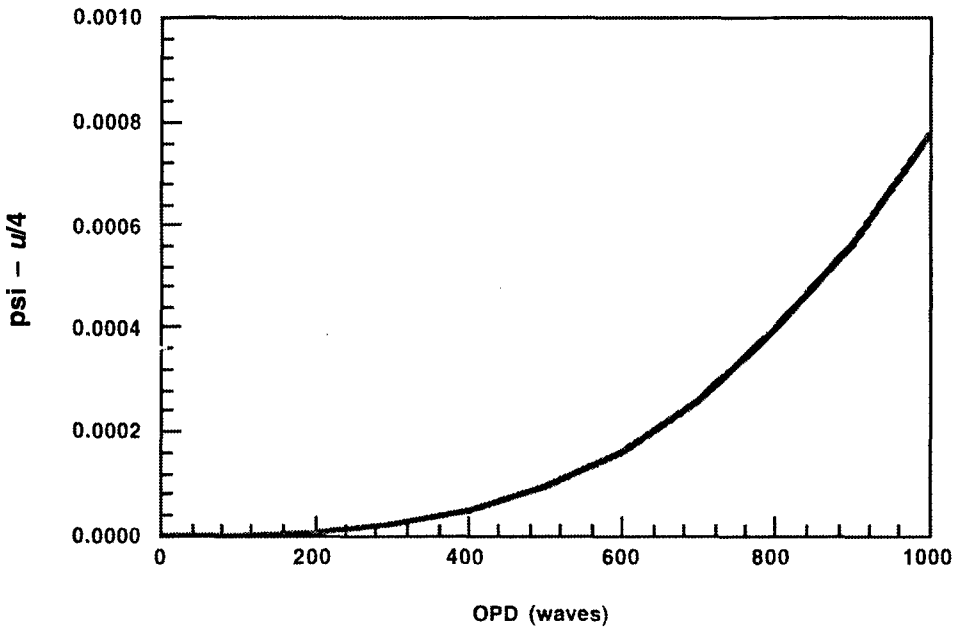

Figure A-2. The residual phase error, in radians, for the GHIS spectrometer, caused by the offset and radius of the detector aperture (field stop).

APPENDIX B

PERMISSIBLE SURFACE ERRORS OF COMPONENTS

It has been shown that the effect of wavefront errors in the Michelson interferometer is to reduce the fringe contrast from its ideal value of one by

$$-\Delta M_{\delta} \approx 2\pi^2 \nu^2 \left\langle \delta^2 \right\rangle \quad , \tag{50}$$

where

$\left\langle \delta^2 \right\rangle$ = the mean-squared value of the wavefront error, or OPD, between interferometer arms, not including the overall optical delay.

Equation (50) can be used as a tool to specify allowable limits on deviation from flatness of the components, individually or as a group. Thus, we need to determine the wavefront errors caused by deviations of each of the surfaces in the interferometer. Figure B-1 shows the optical setup, with labels for each of the surfaces.

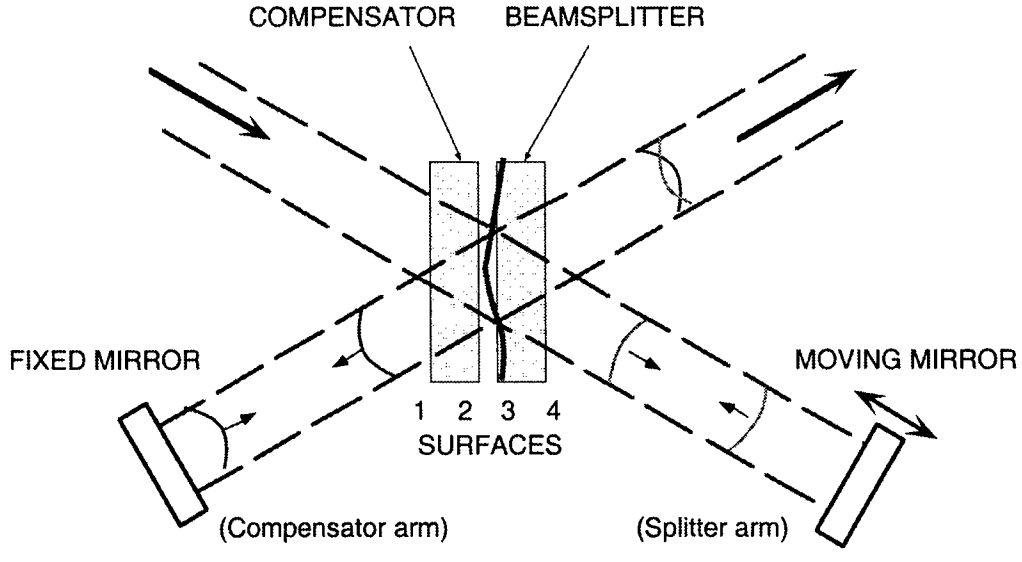

Figure B-1. Typical layout of an unbalanced Michelson interferometer. Wavefront distortions caused by the beamsplitting surface are schematically shown.

Some simple diagrams are helpful for understanding the OPD effect of each surface. Figure B-2 shows rays incident on a refractive element, whose surface is displaced by a distance S in the outward normal direction. Both the refracted and reflected rays are shown. By constructing perpendiculars to the rays at the points of incidence (i.e., parallel to the wavefronts), we can easily deduce the increase in optical path (OPD) caused by displacement S. The formulas for the reflected and refracted rays are shown in the figure. The OPD in the reflected rays is equally applicable to the Michelson mirrors, but in that case we have $\cos\theta = 1$. For refracted rays, the OPD is the same for each direction, and for each face.

Figure B-3 shows the case of rays *internally* reflected from the displaced surface. Otherwise, it is the same as Figure B-2. Notice that the index of refraction changes the OPD effect.

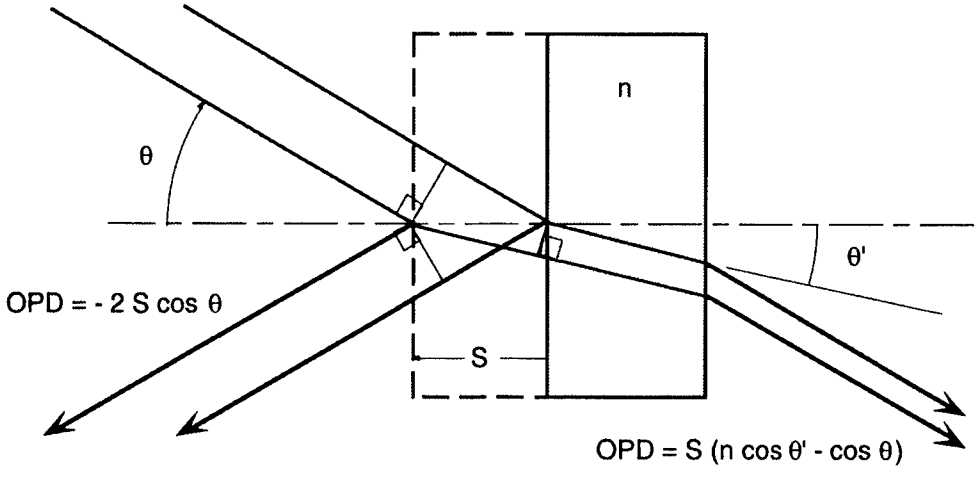

Figure B-2. Geometry of rays refracted and externally reflected from a surface with a positive deviation S. Construction lines are drawn parallel to wavefronts.

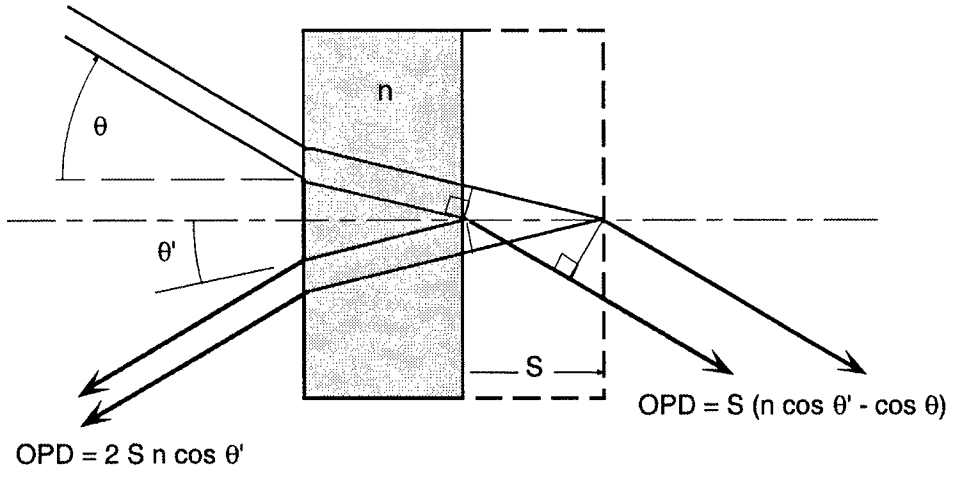

Figure B-3. Geometry of rays refracted and internally reflected from a surface.

For the interferometer shown in Figure B-1, the wavefront OPD between the two arms of the interferometer (except for the overall x) is given by

$$\delta(r,\phi) = 2\left[S_3(n\cos\theta' + \cos\theta) + S_{MS} - S_{MC} + \left(S_4' - S_1' - S_2'\right)(n\cos\theta' - \cos\theta)\right] \quad , \qquad \text{(B-1)}$$

where

θ = the angle of incidence at the beamsplitter,

θ' = the angle of refraction within the beamsplitter and compensator,

n = the index of refraction of the beamsplitter and compensator,

$n\cos\theta' = \sqrt{n^2 - \sin^2\theta}$, from Snell's Law,

S_i = surface deviation of surface i, measured at the ray position (r, ϕ) within the Lyot stop. Primes indicate the non-common ray path intersections.

S_{MS} = surface deviations of the mirror on the beamsplitter side at (r, ϕ), and

S_{MC} = surface deviations of the mirror on the compensator side at (r, ϕ).

In equation (B-1), the position coordinates, (r, ϕ), all refer to a *projected* position within the aperture. We notice that, for small angles of incidence, the OPD is twice as sensitive to beamsplitter errors as to mirror errors. This comes about because a positive surface deviation causes a positive wavefront change in one leg, and a comparable negative change in the other. The optical path difference is roughly twice as large as either. Also, it is the *difference* between the errors on the two mirrors which matters.

Often it is easier to measure (and specify) wavefront irregularity in *transmission*, rather than measure surface irregularity. The transmitted wavefront errors of the compensator and beamsplitter, respectively, are given by

$$\delta_{CT}(r,\phi) = (S_1' + S_2')(n\cos\theta' - \cos\theta) \quad , \text{ and} \tag{B-2}$$

$$\delta_{ST}(r,\phi) = (S_3' + S_4')(n\cos\theta' - \cos\theta) \quad . \tag{B-3}$$

Using these transmitted wavefront errors, equation (B-1) becomes

$$\delta(r,\phi) = 2\left[S_{MS} - S_{MC} + \delta_{ST} - \delta_{CT} + 2S_3\cos\theta\right] \quad . \tag{B-4}$$

Equation (50) can be used to predict the loss of fringe contrast, if we know the exact surface irregularities of the components (using equation B-1), and/or the transmitted wavefront errors (using equation B-4). However, to specify the figure requirements, we must make some simplifying assumptions, as follows. Assume that the figure errors are random and uncorrelated. Their mean-squared values should then be additive. Also, we shall express the errors as *peak-to-valley* (P-V) measurements, given in waves, at some stated test wavelength, λ_{test}. We assume the P-V values to be related to the rms values as

$$F_i \approx \frac{4}{\lambda_{test}}\sqrt{\langle \delta_i^2 \rangle} \quad , \text{ and } \quad W_{jT} \approx \frac{4}{\lambda_{test}}\sqrt{\langle \delta_{jT}^2 \rangle} \tag{B-5a, b}$$

for the flatness of surface i, or the transmitted wavefront error of component j, respectively. Then we find, using equation (B-4),

$$-\Delta M_\delta \approx \frac{\pi^2}{2}\left(\frac{\lambda_{test}}{\lambda}\right)^2\left[F_{MS}^2 + F_{MC}^2 + 4F_3^2\cos^2\theta + W_{ST}^2 + W_{CT}^2\right] \quad , \tag{B-6}$$

where

λ = the (minimum) operating wavelength of the interferometer (= $1/\nu$).

Assuming that both mirrors and both transmissive elements are made to the same specifications, equation (B-6) can be simplified to

$$-\Delta M_\delta < \pi^2\left(\frac{\lambda_{test}}{\lambda}\right)^2\left[F_M^2 + 2F_3^2\cos^2\theta + W_T^2\right] \quad . \tag{B-7}$$

All of the specifications in equation (B-7) must include mounting distortion and thermal effects, as well as the original fabrication errors of the components.

For the case of the GHIS interferometer, $\theta = 30°$, $\lambda \geq 3.7$ μm, and $\lambda_{test} = 0.633$ μm. The beamsplitter and compensator are KBr, with $n(3.7\ \mu\text{m}) = 1.536$. To estimate the wavefront error effects, let us assume that the mirrors are made to 1/4 wave from fabrication, with a further 1/8 wave mounting/thermal distortion. Thus, $F_M \approx 3/8$. For the transmitted wavefronts, assume 1/4 wave from fabrication, and 1/20

wave mounting/thermal distortion. (It is not easy to alter the transmitted wavefront by bending a window.) Thus, $W_T \approx 3/10$. The flatness of the splitter surface is most critical, and we assume 1/8 wave from fabrication plus 1/8 wave distortion, to get $F_3 \approx 1/4$. Inserting these assumptions into (B-7), we find $-\Delta M_\delta < 9.4\%$.

APPENDIX C

MICHELSON INTERFEROMETER WITH RETROREFLECTOR MIRRORS

The plane-mirror Michelson interferometer employed for FT interferometry is sensitive to the angular alignment of its mirrors. A monochromatic interferogram takes the form

$$H_{\varepsilon}(v,x)=\frac{2}{k}J_1(k)\cos(2\pi vx) \quad , \tag{36}$$

where

$$k \equiv 4\pi v \varepsilon R \quad , \tag{37}$$

ε = the tilt misalignment of the mirrors,

R = the radius of the Lyot stop,

v = the wavenumber, and

x = the optical delay.

Tilt misalignment can be avoided by the use of precise retroreflecting optics, such as corner-cube mirrors, or cat's-eye reflectors. A Michelson interferometer with corner-cube retroreflectors is shown schematically in Figure C-1. In principle, retroreflectors return the wavefront exactly parallel to its original plane. However, the returned wavefront is generally inverted in its plane, about the center of the retroreflector. It is shown in this Appendix that this results in a sensitivity of the interferometer to translational alignment of the retroreflectors.

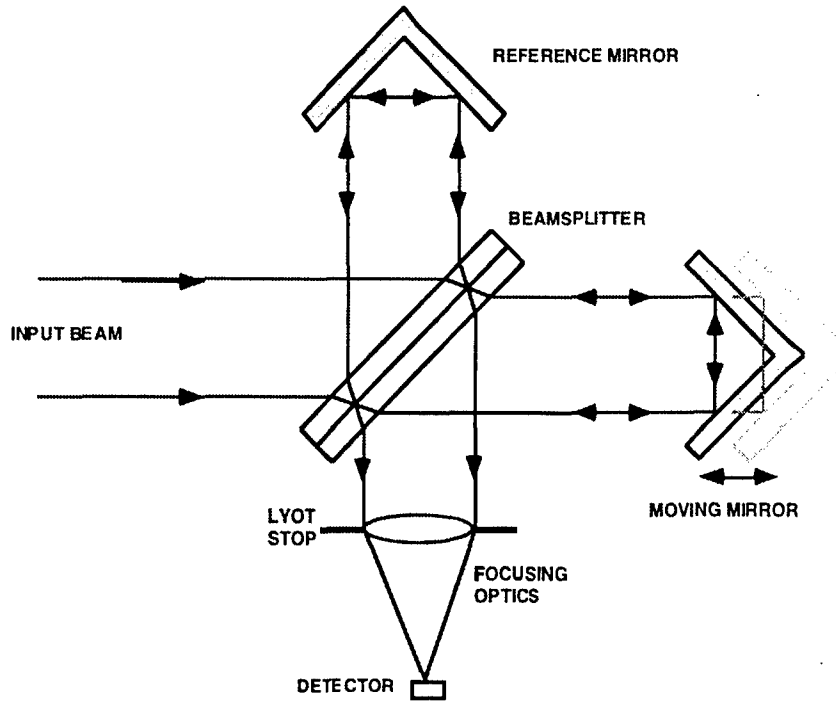

Figure C-1. Michelson interferometer with corner-cube retroreflectors (schematic).

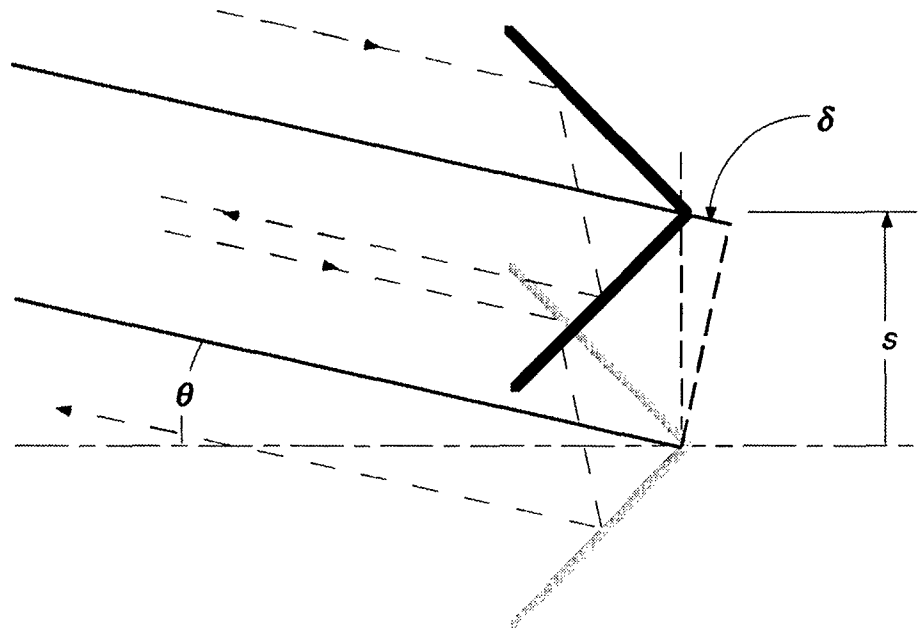

Figure C-2. Close-up of a corner-cube retroreflector which has been displaced from its on-axis position (shown in grey) by distance s. For rays incident at angle θ from the optical axis, the apparent linear shift of the vertex is shown as δ.

C.1 ANALYSIS OF RETROREFLECTOR DISPLACEMENT

Consider now the effects of translational misalignment of the retroreflectors. (We shall assume that the reflectors are optically perfect, i.e., they introduce no wavefront distortions by themselves.) Figure C-2 is a close-up diagram showing one of the retroreflectors displaced a distance s from the optical axis, which is defined by the vertex of the fixed reflector and the center of the Lyot stop. The displacement leaves the incoming and outgoing wavefronts parallel. Also, it has no effect on a beam parallel to the axis. However, for rays incident at an angle θ to the axis, as shown in the figure, there is a change 2δ in the optical path, relative to the undisplaced reflector. The optical delay in the interferometer becomes

$$x' = x\cos\theta + 2\delta = x\cos\theta + 2s\sin\theta \quad , \tag{C-1}$$

or, generalizing to three dimensions,

$$x' = x\cos\rho + 2s\sin\rho\cos\phi \quad , \tag{C-2}$$

where

(ρ, ϕ) = polar and azimuthal angles of rays in the field of view (FOV), and

ϕ = 0 in the displacement direction of retroreflector.

Assume that an extended source of radiation fills the FOV. We need to do an integration over that FOV to obtain the whole signal. The detected signal in the interferometer is

$$s(x) = 2\int_0^\infty S_v\left[1 + H_s(v,x)\right]dv \quad , \tag{C-3}$$

where

$$H_s(v,x) = \frac{1}{\Omega}\int_{-\pi}^{\pi}\int_0^{\rho_0}\cos\left[2\pi v\left(x\cos\rho + 2s\sin\rho\cos\phi\right)\right]\sin\rho\, d\rho\, d\phi \quad , \tag{C-4}$$

ρ_0 = the angular radius of the field of view, and

$\Omega = 2\pi\left(1-\cos\rho_0\right) = 4\pi\sin^2\dfrac{\rho_0}{2}$ = the solid angle of the FOV.

Expanding* the outer cosine in (C-4), we have

$$H_s(v,x) = \frac{1}{\Omega}\left[P_1 - P_2\right] \quad , \tag{C-5}$$

where

$$P_1 = \int_{-\pi}^{\pi}\int_0^{\rho_0}\cos\left(C\cos\rho\right)\cos\left(S\sin\rho\cos\phi\right)\sin\rho\, d\rho\, d\phi \quad , \tag{C-6}$$

$$P_2 = \int_{-\pi}^{\pi}\int_0^{\rho_0}\sin\left(C\cos\rho\right)\sin\left(S\sin\rho\cos\phi\right)\sin\rho\, d\rho\, d\phi \quad , \tag{C-7}$$

*Readers of Appendix A will recognize that the integral in equation (C-4) is identical in form to that in equation (A-2), and anticipate that the solution will be in terms of Lommel functions.

and the expressions have been simplified by defining $C \equiv 2\pi vx$ and $S \equiv 4\pi vs$. We observe that since the integrand in equation (C-7) is antisymmetric in ϕ, we have $P_2 = 0$. When we make use of

$$\int_0^{\pi} \cos(x\cos\phi)d\phi = \pi J_0(x) \quad ,$$

the ϕ integration in P_1 yields

$$P_1 = 2\pi\int_0^{\rho_0} \cos(C\cos\rho)J_0(S\sin\rho)\sin\rho\, d\rho \quad . \tag{C-8}$$

Proceeding as in Appendix A, make the substitution

$$\sin\rho \equiv r\sin\rho_0 \quad , \quad \cos\rho = \sqrt{1-r^2\sin^2\rho_0} \approx 1-\frac{1}{2}r^2\sin^2\rho_0 \quad ,$$

and the approximation

$$\sin\rho\, d\rho = \frac{r dr \sin^2\rho_0}{\sqrt{1-r^2\sin^2\rho_0}} \approx r dr \sin^2\rho_0 \quad .$$

Thus equation (C-8) becomes

$$P_1 \approx 2\pi\sin^2\rho_0\int_0^1 \cos\left(C\left[1-\frac{1}{2}r^2\sin^2\rho_0\right]\right)J_0(Sr\sin\rho_0)r\, dr \quad . \tag{C-9}$$

Defining the symbols

$$u \equiv C\sin^2\rho_0 \text{ and } w \equiv S\sin\rho_0 \quad ,$$

and expanding the cosine, we have

$$P_1 \approx \pi\sin^2\rho_0\left[A(u,w)\cos C + B(u,w)\sin C\right] \quad , \tag{C-10}$$

where

$$A(u,w) \equiv 2\int_0^1 \cos\left(\frac{1}{2}ur^2\right)J_0(wr)r\, dr \quad , \text{ and} \tag{C-11a}$$

$$B(u,w) \equiv 2\int_0^1 \sin\left(\frac{1}{2}ur^2\right)J_0(wr)r\, dr \quad . \tag{C-11b}$$

Since we have

$$\pi\sin^2\rho_0 \approx \Omega \quad , \tag{C-12}$$

equations (C-10) and (C-5) combine (since $P_2 = 0$) to give

$$H_s(v,x) \approx A(u,w)\cos C + B(u,w)\sin C \quad . \tag{C-13}$$

Once again, the two r integrals in equations (C-11) yield a solution in terms of *Lommel functions* [13] (Section 8.8.1., pp. 435-439). The Lommel functions are defined as

$$U_n(u,w) = \sum_{s=0}^{\infty} (-1)^s \left(\frac{u}{w}\right)^{n+2s} J_{n+2s}(w) \quad , \text{ and} \tag{C-14a}$$

$$V_n(u,w) = \sum_{s=0}^{\infty} (-1)^s \left(\frac{w}{u}\right)^{n+2s} J_{n+2s}(w) \quad . \tag{C-14b}$$

So far, the solution has paralleled that in Appendix A; but here we are interested in the case where the retroreflector displacement, s, is small, but the OPD may be large, such that $w/u < 1$. Thus we need a solution in terms of the V_n series. From Born and Wolf [13], we find

$$A(u,w) = \frac{2}{u}\sin\frac{w^2}{2u} + \frac{\sin\frac{1}{2}u}{\frac{1}{2}u} V_0(u,w) - \frac{\cos\frac{1}{2}u}{\frac{1}{2}u} V_1(u,w) \quad , \text{ and} \tag{C-15a}$$

$$B(u,w) = \frac{2}{u}\cos\frac{w^2}{2u} - \frac{\cos\frac{1}{2}u}{\frac{1}{2}u} V_0(u,w) - \frac{\sin\frac{1}{2}u}{\frac{1}{2}u} V_1(u,w) \quad . \tag{C-15b}$$

Inserting these solutions in (C-13) and collecting trigonometric factors, we find

$$H_s(v,x) \approx \frac{2}{u}\left[\sin\left(C + \frac{w^2}{2u}\right) - \sin\left(C - \frac{u}{2}\right)V_0(u,w) - \cos\left(C - \frac{u}{2}\right)V_1(u,w)\right] \quad . \tag{C-16}$$

Though it is a solution in closed form, the result in (C-16) needs further reduction before it can easily be compared with the more usual expressions. We may define intermediate symbols

$$Y \equiv C - \frac{u}{2} \quad , \textit{ and } \quad Z \equiv \frac{u}{2} + \frac{w^2}{2u} \quad ,$$

and (C-16) becomes

$$H_s(v,x) \approx \frac{2}{u}\left[\sin(Y+Z) - \sin Y V_0(u,w) - \cos Y V_1(u,w)\right] \quad . \tag{C-17}$$

Next we have

$$H_s(v,x) \approx \frac{2}{u}\left\{\sin Y\left[\cos Z - V_0(u,w)\right] + \cos Y\left[\sin Z - V_1(u,w)\right]\right\} \quad , \tag{C-18}$$

which can be written

$$H_s(v,x) \approx M(u,w)\left[\sin Y \sin\psi + \cos Y \cos\psi\right] = M(u,w)\cos(Y-\psi) \quad , \tag{C-19}$$

where we define (omitting the explicit Lommel function arguments for brevity),

$$M(u,w) \equiv \frac{2}{u}\sqrt{1+V_0^2+V_1^2-2V_0\cos Z-2V_1\sin Z} \quad , \text{ and} \tag{C-20a}$$

$$\tan\psi \equiv \frac{\cos Z - V_0}{\sin Z - V_1} \quad . \tag{C-20b}$$

The foregoing solution is equivalent to that given by Murty [14] for the same case of $w < u$.

At this point, we return to the definitions of u, w, Y, Z, etc.:

$$u \equiv C\sin^2\rho_0 = 2\pi vx\sin^2\rho_0 \quad , \tag{C-21a}$$

$$w \equiv S\sin^2\rho_0 = 4\pi vs\sin\rho_0 \quad , \tag{C-21b}$$

$$Y = 2\pi vx\left(1-\frac{1}{2}\sin^2\rho_0\right) = 2\pi vx\left(1-\frac{\Omega}{2\pi}\right) \quad , \text{ and} \tag{C-21c}$$

$$Z = 2\pi vx\left(\frac{1}{2}\sin^2\rho_0 + 2\left(\frac{s}{x}\right)^2\right) = 2\pi vx\left(\frac{\Omega}{2\pi} + 2\left(\frac{s}{x}\right)^2\right) \quad . \tag{C-21d}$$

In these expressions, we have made use of

$$\sin^2\rho_0 \approx \frac{\Omega}{\pi} \quad .$$

Equation (C-19) is seen to be

$$\boxed{H_s(v,x) \approx M(u,w)\cos\left(2\pi vx\left(1-\frac{\Omega}{2\pi}\right)-\psi\right) \quad .} \tag{C-22}$$

We recognize that (C-22) is very similar in form to equation (24) in Section 3.2, namely a fringe cosine, modulated by a slowly-varying factor, M. The argument of the cosine is modified with the same factor as in (24), but an additional phase shift (ψ) appears.

The modulation factor M and phase shift ψ have been evaluated for the case of ρ_0 = 1°, and vx = 1,000 waves. The results are plotted as a function of vs (the displacement in waves) in Figures C-3 and C-4.

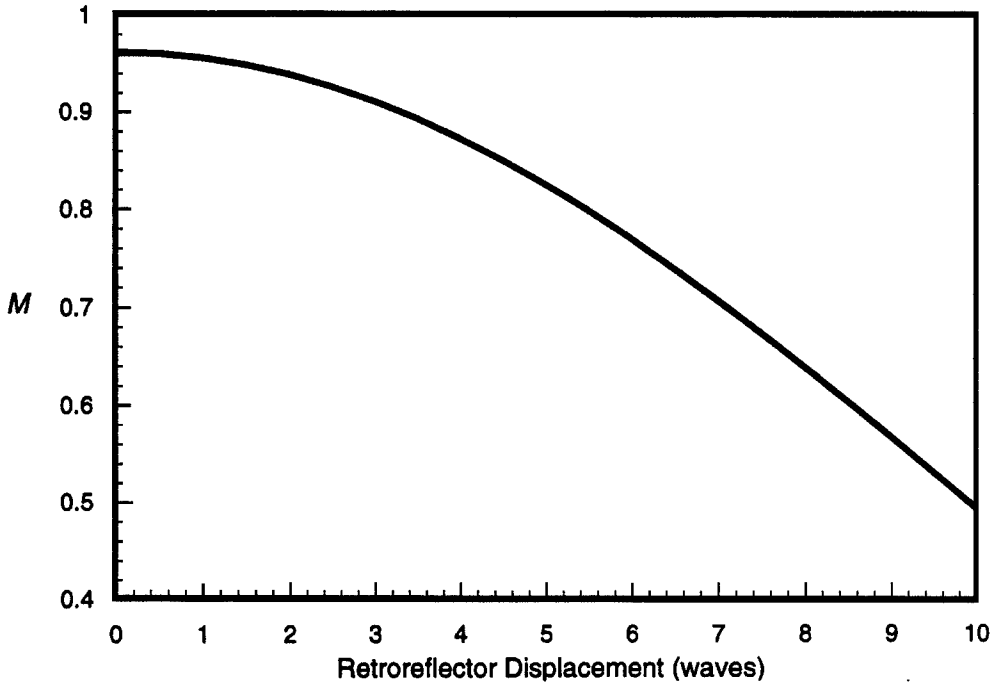

Figure C-3. Modulation factor M(u, w), vs. retroreflector displacement, vs (in waves), for the case of FOV radius ρ_0 = 1°, and the interferometer OPD vx = 1,000 waves (u = 1.91).

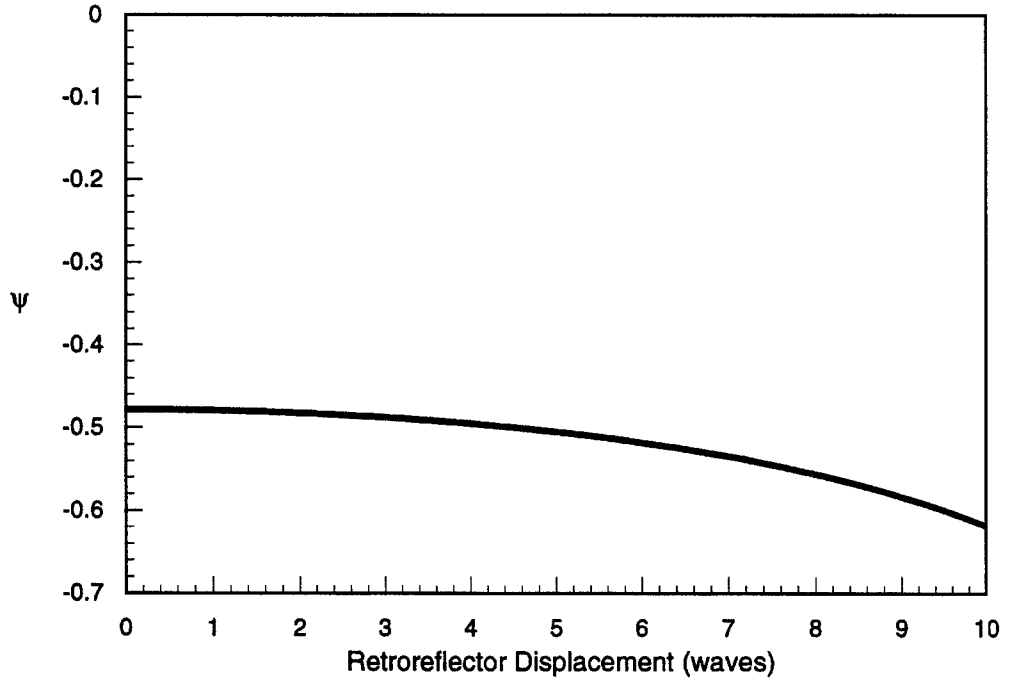

Figure C-4. Phase shift ψ(u, w) vs. retroreflector displacement, vs (in waves), for the same case as in Figure C-3.

As a check on the foregoing result, we observe that for $s = 0$, then $w = 0$, $V_0(u,0) = 1$, and $V_1(u,0) = 0$. Equation (C-16) becomes

$$H_s(v,x) \approx \frac{2}{u}[\sin(Y+Z) - \sin Y] = \frac{4}{u}\cos\left(Y+\frac{1}{2}Z\right)\sin\left(\frac{1}{2}Z\right) \quad , \text{ or} \tag{C-23}$$

$$H_s(v,x) \approx \frac{4}{u}\sin\left(\frac{u}{4}\right)\cos\left(C-\frac{u}{4}\right) = \text{sinc}\left(\frac{u}{4\pi}\right)\cos\left(C-\frac{u}{4}\right) \quad . \tag{C-24}$$

Inserting the definitions above,

$$H_s(v,x) \approx \text{sinc}\left(vx\frac{\Omega}{2\pi}\right)\cos\left(2\pi vx\left[1-\frac{\Omega}{4\pi}\right]\right) \quad , \tag{C-25}$$

which is identical to equation (24), and represents the apodization caused by the extended field of view.

C.2 APPROXIMATE EXPRESSIONS FOR THE FRINGE MODULATION

To clarify the behavior of the amplitude modulation and phase factors, we may express them as power series expansions, valid for small s. We use the series for the Bessel functions

$$J_n(w) = \left(\frac{w}{2}\right)^n \sum_{k=0}^{\infty} \frac{(-1)^k}{k!(n+k)!}\left(\frac{w}{2}\right)^{2k} \approx \frac{1}{n!}\left(\frac{w}{2}\right)^n \quad .$$

Thus to first order in $(w/2)^2$,

$$V_0(u,w) \approx 1-\left(\frac{w}{2}\right)^2 \quad , \text{ and } \quad V_1(u,w) \approx \frac{2}{u}\left(\frac{w}{2}\right)^2 \quad . \tag{C-26a,b}$$

Inserting these approximations in (C-20a), we find

$$M(u,w) \approx \frac{2}{u}\sqrt{2[1-\cos Z]\left[1-\left(\frac{w}{2}\right)^2\right] - \frac{4}{u}\left(\frac{w}{2}\right)^2 \sin Z} \quad . \tag{C-27}$$

Applying the identities

$$\sin^2\frac{Z}{2} = \frac{1-\cos Z}{2} \quad \text{and} \quad \cot\frac{Z}{2} = \frac{\sin Z}{1-\cos Z} \quad , \tag{C-28}$$

we find

$$M(u,w) \approx \frac{4}{u}\sin\frac{Z}{2}\left[1-\left(\frac{w}{2}\right)^2\left(1+\frac{2}{u}\cot\frac{Z}{2}\right)\right]^{\frac{1}{2}} \approx \frac{4}{u}\sin\frac{Z}{2}\left[1-\frac{1}{2}\left(\frac{w}{2}\right)^2\left(1+\frac{2}{u}\cot\frac{Z}{2}\right)\right] \quad . \tag{C-29}$$

From the definition of Z,

$$\sin\frac{Z}{2}=\sin\frac{u}{4}\cos\frac{w^2}{4u}+\cos\frac{u}{4}\sin\frac{w^2}{4u} \quad , \tag{C-30}$$

or, since w is small (though u may be appreciable),

$$\sin\frac{Z}{2}=\sin\frac{u}{4}+\frac{w^2}{4u}\cos\frac{u}{4}=\sin\frac{u}{4}\left[1+\frac{1}{u}\left(\frac{w}{2}\right)^2\cot\frac{u}{4}\right] \quad . \tag{C-31}$$

Making the substitution in (C-29), we get

$$M(u,w)\approx\frac{4}{u}\sin\frac{u}{4}\left[1+\frac{1}{u}\left(\frac{w}{2}\right)^2\cot\frac{u}{4}\right]\left[1-\frac{1}{2}\left(\frac{w}{2}\right)^2\left(1+\frac{2}{u}\cot\frac{Z}{2}\right)\right] \quad , \tag{C-32}$$

or

$$M(u,w)\approx\frac{4}{u}\sin\frac{u}{4}\left[1-\frac{1}{2}\left(\frac{w}{2}\right)^2+\frac{1}{u}\left(\frac{w}{2}\right)^2\left(\cot\frac{u}{4}-\cot\frac{Z}{2}\right)\right] \quad . \tag{C-33}$$

From the identity

$$\cot A-\cot B=\frac{\sin(B-A)}{\sin A\sin B} \quad ,$$

we find that

$$\cot\frac{u}{4}-\cot\frac{Z}{2}=\frac{\sin\left(\frac{w^2}{4u}\right)}{\sin\frac{u}{4}\sin\left(\frac{u}{4}+\frac{w^2}{4u}\right)}\approx\frac{\frac{1}{u}\left(\frac{w}{2}\right)^2}{\sin^2\frac{u}{4}} \quad . \tag{C-34}$$

Hence, the third term in (C-33) is second order in $(w/2)^2$, and we obtain

$$\boxed{M(u,w)\approx\frac{4}{u}\sin\frac{u}{4}\left[1-\frac{w^2}{8}\right] \quad .} \tag{C-35}$$

For the phase shift, ψ, we have from equation (C-20b), to first order in $(w/2)^2$,

$$\tan\psi\approx\frac{\cos Z-1+\left(\frac{w}{2}\right)^2}{\sin Z-\frac{2}{u}\left(\frac{w}{2}\right)^2} \quad , \tag{C-36}$$

which may be expressed as

$$\tan\psi \approx \frac{\cos Z - 1}{\sin Z}\left[1+\left(\frac{w}{2}\right)^2 \frac{1}{\cos Z - 1}\right]\left[1-\frac{2}{u}\left(\frac{w}{2}\right)^2 \frac{1}{\sin Z}\right]^{-1} \quad , \tag{C-37}$$

or

$$\tan\psi \approx -\left[1+\left(\frac{w}{2}\right)^2\left(\frac{1}{\cos Z - 1}+\frac{2}{u}\frac{1}{\sin Z}\right)\right]\tan\frac{Z}{2} \quad , \tag{C-38}$$

or also

$$\tan\psi \approx -\left[1+\frac{2}{u}\frac{1}{\sin Z}\left(\frac{w}{2}\right)^2\right]\tan\frac{Z}{2}+\frac{1}{\sin Z}\left(\frac{w}{2}\right)^2 \quad . \tag{C-39}$$

Let us assume that

$$\tan\psi = \tan\left(\chi - \frac{Z}{2}\right) = \frac{\tan\chi - \tan\frac{Z}{2}}{1+\tan\chi\tan\frac{Z}{2}} \quad . \tag{C-40}$$

To find χ, we compare (C-39) and (C-40) to find that

$$\tan\chi \approx \frac{\left(\frac{w}{2}\right)^2}{\sin Z+\frac{2}{u}\left(\frac{w}{2}\right)^2} \approx \frac{1}{\sin Z}\left(\frac{w}{2}\right)^2 \quad . \tag{C-41}$$

Hence, to first order we have

$$\chi \approx \frac{1}{\sin Z}\left(\frac{w}{2}\right)^2 \quad , \tag{C-42}$$

and

$$\boxed{\psi \approx -\frac{Z}{2}+\frac{1}{\sin Z}\left(\frac{w}{2}\right)^2 = -\frac{u}{4}+\left(\frac{1}{\sin Z}-\frac{1}{u}\right)\left(\frac{w}{2}\right)^2} \quad . \tag{C-43}$$

Gathering together equations (C-19), (C-35), and (C-43), we have the approximate expression for H_s, for small values of s:

$$H_s(v,x) \approx \frac{4}{u}\sin\frac{u}{4}\left[1-\frac{w^2}{8}\right]\cos\left(C-\frac{u}{4}-\left(\frac{1}{\sin Z}-\frac{1}{u}\right)\left(\frac{w}{2}\right)^2\right) \quad . \tag{C-44}$$

We observe that equation (C-44) is of almost exactly the same form as (C-24) or (24) of Section 3.2, with the addition of an amplitude modulation factor and an additional phase shift. The factor

$$1-\frac{w^2}{8} = 1-2\pi^2(vs)^2\sin^2\rho_0 = 1-2\pi(vs)^2\Omega \tag{C-45}$$

represents the loss of fringe contrast caused by the retroreflector displacement alone.

C.3 RETROREFLECTORS VS PLANE MIRRORS

An obvious question arises as to whether better interferometer performance can be obtained with plane mirrors or with retroreflectors, given the level of alignment precision that is attainable. For the plane-mirror interferometer, the expression for loss of fringe contrast corresponding to (C-45) is

$$\frac{2}{k}J_1(k) = 1-\frac{1}{2}\left(\frac{k}{2}\right)^2+\frac{1}{12}\left(\frac{k}{2}\right)^4-\cdots \approx 1-2(\pi v\varepsilon R)^2 \quad , \tag{38}$$

where R is the radius of the Lyot stop, and ε is the mirror tilt error. If we define the respective losses of fringe contrast as

$$\Delta_{retro} \equiv 2\pi^2(vs)^2\sin^2\rho_0, \text{ and } \Delta_{plane} \equiv 2(\pi v\varepsilon R)^2 \quad ,$$

and take their ratio, we find

$$\frac{\Delta_{retro}}{\Delta_{plane}} = \left(\frac{s\sin\rho_0}{\varepsilon R}\right)^2 \quad . \tag{C-46}$$

For any interferometer with given R and ρ_0, equation (C-46) expresses the relative sensitivity to loss of fringe contrast caused by displacement error for retroreflectors vs tilt error for flat mirrors.

To put the loss ratio in perspective, let us assume that parts can be positioned with a linear precision of s, and with an angular precision of s/D, where D is a characteristic size. Let us take D to be the diameter of the Lyot stop. In this case, the plane mirrors contrast loss is

$$\Delta_{plane} = \frac{1}{2}(\pi vs)^2 \quad , \tag{C-47}$$

and the ratio of losses becomes

$$\frac{\Delta_{retro}}{\Delta_{plane}} = 4\sin^2\rho_0 \quad . \tag{C-48}$$

We can conclude that $\Delta_{retro} < \Delta_{plane}$ as long as $\rho_0 < 30°$. In words, the retroreflector misalignment will cause less loss of fringe contrast than plane-mirror misalignment under these assumptions, as long as the field-of-view diameter is less than 60°. Since this is almost certain to be true, we are led to believe that it is easier to build a high-performance interferometer with retroreflectors, rather than plane mirrors.

The foregoing conclusion must be tempered with the fact that it is much more difficult to fabricate an ideal retroreflector than an ideal plane mirror. A complete trade study must also take into account the wavefront errors likely to be introduced by the different components. Furthermore, the ratio of the linear and angular positioning errors may be quite different than assumed above, when the details of the Michelson mirror scan motion are accounted for.

REFERENCES

1. *High-Resolution Interferometer Modification of the GOES L/M Sounder: Feasibility Study*, University of Wisconsin-Madison Cooperative Institute for Meteorological Satellite Studies (CIMSS), Santa Barbara Research Center (Hughes/SBRC), ITT Aerospace/Optical Division, RPT81280, September 1988.

2. W. E. Bicknell, J. W. Burnside, L. M. Candell, H. W. Feinstein, D. R. Hearn, J. P. Kerekes, A. B. Plaut, D. Ryan-Howard, W. J. Scouler, and D. E. Weidler, GOES *High-Resolution Interferometer Sounder Study*, MIT Lincoln Laboratory, Project Report NOAA-12, 5 June 1995.

3. D. L. Mooney, D. L. Bold, M. S. Cafferty, D. L. Cohen, H. J. Jimenez, J. P. Kerekes, R. W. Miller, M. J. Persky, and D. P. Ryan-Howard, *POES Advanced Sounder Study (Phase II)*, MIT Lincoln Laboratory, Project Report NOAA-7, 17 March 1994.

4. R. J. Bell, *Introductory Fourier Transform Spectroscopy*, Academic Press, New York (1972).

5. J. W. Brault, *Fourier Transform Spectrometry*, National Solar Observatory, Tucson (1984).

6. R. Kingslake, *Optical System Design* (1983).

7. H. B. Dwight, *Tables of Integrals and Other Mathematical Data*, MacMillan (1961).

8. *The Infrared Handbook, Revised Edition*, W. L. Wolfe and G. J. Zissis, Eds., Environmental Research Institute of Michigan (1985).

9. R. N. Bracewell, *The Fourier Transform and its Applications*, McGraw-Hill (1965).

10. E. E. Bell and R. B. Sanderson, *Applied Optics*, Vol. 11, pp. 688-689 (March 1972).

11. A. S. Zachor, *Applied Optics*, Vol. 16, pp. 1412-1424 (May 1977).

12. H. Revercomb, University of Wisconsin, private communication (13 July 1992).

13. M. Born and E. Wolf, *Principles of Optics*, 6th Edition, Pergamon (1980).

14. M. V. R. K. Murty, "Some More Aspects of the Michelson Interferometer with Cube Corners," *Journal of the Optical Society of America*, Vol. 50, pp. 7-10 (January 1960).

REPORT DOCUMENTATION PAGE

Form Approved
OMB No. 0704-0188

1. AGENCY USE ONLY (*Leave blank*)	2. REPORT DATE	3. REPORT TYPE AND DATES COVERED
	29 October 1999	Technical Report

4. TITLE AND SUBTITLE

Fourier Transform Interferometry

5. FUNDING NUMBERS

C — F19628-95-C-0002
PR — 460

6. AUTHOR(S)

David R. Hearn

7. PERFORMING ORGANIZATION NAME(S) AND ADDRESS(ES)

Lincoln Laboratory, MIT
244 Wood Street
Lexington, MA 02420-9108

8. PERFORMING ORGANIZATION REPORT NUMBER

TR-1053

9. SPONSORING/MONITORING AGENCY NAME(S) AND ADDRESS(ES)

National Oceanic and Atmospheric Administration
1315 East West Highway
Silver Spring, MD 20910

10. SPONSORING/MONITORING AGENCY REPORT NUMBER

ESC-TR-98-052

11. SUPPLEMENTARY NOTES

None

12a. DISTRIBUTION/AVAILABILITY STATEMENT

Approved for public release; distribution is unlimited.

12b. DISTRIBUTION CODE

13. ABSTRACT (*Maximum 200 words*)

The basic Michelson interferometer, as used for Fourier transform spectroscopy, is analyzed in this report. The principles of operation are explained, and its inherent limitations are shown. An original analysis of apodization, for the case of an off-axis detector field-of-view, is included in an appendix. Practical limitations of real instruments are also analyzed. These include misalignment, wavefront error, and noise sources. In another appendix, the use of retroreflectors in the interferometer is analyzed, and the effect of lateral displacement of a retroreflector is compared to that of mirror tilt in a plane-mirror interferometer. Special attention is given to sources of noise in the Fourier transform spectroradiometer, and expressions are derived for noise-equivalent radiance from these sources. The performance of a Fourier transform spectrometer is compared with that of a filter-wheel spectrometer having the same optical aperture and spectral resolution. The mathematical treatments in this report are sufficiently detailed that they should be easy to follow, once the optical principles are grasped. Some numerical calculations are included, based on the specifications of the proposed GOES High-Resolution Interferometer Sounder (GHIS).

14. SUBJECT TERMS

interferometer
Michelson
spectroscopy
spectrometer
FTIR
Fourier transform

15. NUMBER OF PAGES
70

16. PRICE CODE

17. SECURITY CLASSIFICATION OF REPORT	18. SECURITY CLASSIFICATION OF THIS PAGE	19. SECURITY CLASSIFICATION OF ABSTRACT	20. LIMITATION OF ABSTRACT
Unclassified	Unclassified	Unclassified	Same as Report